Geophysical Journal International

Geophys. J. Int. (2012) doi: 10.1111/j.1365-246X.2012.05499.x

Normal mode sensitivity to Earth's D″ layer and topography on the core–mantle boundary: what we can and cannot see

P. J. Koelemeijer,[1] A. Deuss[1] and J. Trampert[2]

[1] *Bullard Laboratories, University of Cambridge, Madingley Road, Cambridge* CB3 0EZ, *UK. E-mail: pjk49@cam.ac.uk*
[2] *Department of Earth Sciences, Utrecht University, PO Box* 80021, 3508 *TA Utrecht, The Netherlands*

Accepted 2012 April 15. Received 2012 March 28; in original form 2011 November 25

SUMMARY

The core–mantle boundary (CMB) is Earth's most profound internal boundary separating the liquid iron outer core and the solid silicate mantle. The detailed structure near the CMB has a major influence on mantle convection and the evolution of the core. Seismic observations, such as topography on the CMB, thin ultra-low velocity zones (ULVZs), seismic anisotropy and the anticorrelation between shear wave and bulk sound velocity heterogeneities have mainly been made using body waves and are still poorly constrained. We investigate the sensitivity of Earth's free oscillations to these features and specifically show how large individual anomalies must be for them to be observable. In addition, we discuss the possible trade-offs between these different lowermost mantle structures. Although modes have strong sensitivity to all the structures inserted, the results illustrate the limits of what normal modes can resolve. Our tests show that: (i) Even small scale features, such as ULVZs, with a thickness larger than 19 km can be observed as long as their distribution contains a long wavelength component. (ii) The peak-to-peak amplitude of CMB topography has a larger influence than its pattern and has to be smaller than 5 km to fit the data. (iii) The effect of scaling between shear wave velocity and density anomalies is less constrained, but a laterally varying pattern is implied by a simple test, suggesting the presence of chemical variations. (iv) A strong trade-off exists between anisotropy in compressional wave velocity and incidence angle whereas shear wave anisotropy is less observable. These findings provide valuable information for future normal mode studies on structures in Earth's lowermost mantle and their trade-offs.

Key words: Mantle processes; Composition of the mantle; Surface waves and free oscillations; Seismic anisotropy; Theoretical seismology.

1 INTRODUCTION

Earth's largest thermal and compositional interface is the core–mantle boundary (CMB) at nearly 2900 km depth (Dziewonski & Anderson 1981). The lowermost 200–300 km of the mantle, referred to as the D″ layer, is generally more complex and anomalous than the rest of the mantle (e.g. Lay *et al.* 1998; Lay 2007; Garnero & McNamara 2008; Lay & Garnero 2011). This region is believed to act as a thermal boundary layer and is an important factor in controlling mantle convection. The D″ region also plays an important role in segregating chemical heterogeneities for long periods of time (Lay 2007; Garnero & McNamara 2008); it could have a profound effect on the evolution and growth of the inner core (Hide *et al.* 1993; Lay 2007) and its observed anisotropy by regulating the core heat flux (Aubert *et al.* 2008).

The most prominent structure found in the D″ is the occurrence of large low shear wave velocity provinces (LLSVPs) underneath the South Pacific and Africa which might reflect dynamically stable, chemically distinct material (Deschamps *et al.* 2007; Garnero & McNamara 2008; McNamara *et al.* 2010; Lay & Garnero 2011). The observation of an anticorrelation between variations in the seismic shear ($\delta \ln V_s$) and bulk sound ($\delta \ln V_\phi$) velocities in these regions suggests furthermore that chemical variations occur. This anticorrelation is observed both on a global scale in tomographical models (Su & Dziewonski 1997; Kennett *et al.* 1998; Ishii & Tromp 1999) and on a local scale by body wave studies which show abrupt anticorrelated jumps in the seismic velocities (e.g. Van der Hilst *et al.* 2007; Hutko *et al.* 2008; Chaloner *et al.* 2009). The likelihood of low or negative correlations between $\delta \ln V_s$ and $\delta \ln \rho$ seems large (Resovsky & Trampert 2003), which has been interpreted as variations in iron content (Forte & Mitrovica 2001). In recent years, a deep mantle phase transition from perovskite to post-perovskite has been discovered (e.g. Murakami *et al.* 2004; Oganov & Ono 2004; Hirose 2006) which has been suggested as an explanation for some of the seismic observations in the D″ region (Van der Hilst *et al.* 2007; Hutko *et al.* 2008).

Thin layers (4–50 km thick), referred to as ultra-low velocity zones (ULVZs), with reductions in shear (S) and compressional (P)

wave velocity up to −30 and −10 per cent, respectively, have been detected just atop the CMB (e.g. Garnero *et al.* 1998; Lay & Garnero 2011). ULVZs have been found mostly beneath the Central-South Pacific and the South Atlantic (Castle *et al.* 2000; Thorne & Garnero 2004; Rondenay *et al.* 2010) whereas evidence is often lacking in the Northern Atlantic (Thorne & Garnero 2004; Rost *et al.* 2010). Their thickness is typically less than ∼12 km, which makes detection challenging. Also, ULVZ thickness trade-offs with the amplitude of the velocity reductions (Thorne & Garnero 2004). The observed reductions, with a typical 3:1 ratio for the *S*- to- *P*-wave velocity, are much greater than those suggested by tomographical models. Hence, a partial melting origin has generally been inferred (e.g. Thorne & Garnero 2004; Rost *et al.* 2005; Stixrude & Karki 2005; Garnero & McNamara 2008), supported by the observation that their occurrence appears to correlate with hotspot locations (Williams *et al.* 1998). Recent work shows that the ULVZ material might also be chemically different and could be present as dynamically long-lived structures in relation to chemically distinct LLSVPs (McNamara *et al.* 2010).

Further complexities in D″ arise from the observation of large-scale regions with apparent seismic anisotropy (Montagner 1998), which have been found in both global studies (Montagner & Kennett 1996; Beghein *et al.* 2006) and local body wave studies using *S*-wave splitting (e.g. Moore *et al.* 2004; Long 2009; Nowacki *et al.* 2010). Radial anisotropy in D″ is most pronounced in *P*-wave velocity with *S*-wave velocity anisotropy being less strong (Montagner & Kennett 1996; Beghein *et al.* 2006). Regional studies have inferred mainly vertical transverse isotropy of a few percent for *S*-wave splitting (Moore *et al.* 2004). This deep anisotropy has been explained by flow aligned crystals (Kendall & Silver 1996) or aligned melt inclusions (Kendall & Silver 1996; Moore *et al.* 2004). More recently, it has been explained by post-perovskite which has intrinsic anisotropy (Nowacki *et al.* 2010) or by flow induced deformation (Panning & Romanowicz 2006; Wenk *et al.* 2011).

In addition to complexities found in the D″ layer, dynamic topography on the CMB itself has been observed in studies using body waves (e.g. Morelli & Dziewonski 1987; Boschi & Dziewonski 2000; Sze & van der Hilst 2003), normal modes (Li *et al.* 1991b; Ishii & Tromp 1999), convection modelling (e.g. Forte 2007; Simmons *et al.* 2009; Lassak *et al.* 2010) and rotational data (e.g. Hager *et al.* 1985; Jault & Le Mouël 1990). Long wavelength (∼4000 km) CMB topography estimates are 4–10 km in amplitude and short wavelength variations (∼10 km) are thought to be less then 300 m (Souriau 2007). Although several studies show a 'Ring around the Pacific' pattern, with relatively large regions of elevated topography in the Central Pacific surrounded by depressed topography (Li *et al.* 1991b; Forte 2007; Simmons *et al.* 2009; Lassak *et al.* 2010), most studies differ in detail. At present, consensus regarding the regional pattern of the CMB topography, as well as on its peak-to-peak amplitude is lacking.

In this study, we use Earth's free oscillations (or normal modes) to investigate how strongly anomalous and how widespread these lowermost mantle features need to be in order to be observable in present normal mode data and what trade-offs are present between different structures. The use of normal modes has many advances over body waves. Long period data are global in character and normal modes are sensitive to density variations in addition to velocity. In addition, no approximations are required to calculate full waveforms. It is still unclear whether ULVZs in the D″ layer can also be seen with normal modes as normal modes are sensitive to the entire Earth. Furthermore, it is important to quantify trade-offs between all the lowermost mantle features. Therefore, we will investigate, for the first time, the sensitivity of modes to ULVZs and study in detail what D″ structures normal modes can resolve.

2 NORMAL MODE THEORY

Earth's normal modes or free oscillations are standing waves arising along the surface and radius of the Earth. Normal modes are observed after large earthquakes which make the Earth ring like a bell. Due to the finite size of the Earth, only discrete frequencies are permitted, determined by the velocity structure and density distribution in the Earth. Spheroidal mode multiplets ${}_nS_l$ and toroidal mode multiplets ${}_nT_l$ are characterized by their radial order n and angular order l. Each normal mode consists of $2l+1$ singlets with azimuthal order m in the range $-l, \ldots, l$. These singlets are degenerate (i.e. have the same frequency) for a spherically symmetric, isotropic, non-rotating earth model such as the Preliminary Reference Earth Model (PREM; Dziewonski & Anderson 1981). Significant splitting of the singlets into different frequencies occurs by the rotation and ellipticity of the Earth, which explains the fundamental mode data reasonably well (Fig. 1). Observed additional splitting is due to velocity and density heterogeneity, anisotropy and topography on internal boundaries in the Earth. Incorporating splitting due to heterogeneous mantle structure in addition to rotation and ellipticity visibly improves the fit to the data, as is observed for mantle modes ${}_1S_{10}$, ${}_4S_3$ and ${}_4S_4$ in Fig. 1.

Splitting function coefficients were introduced by Woodhouse *et al.* (1986) as a convenient way to describe the splitting of normal modes in a complete way. Perturbation theory is used to relate these coefficients, denoted as c_{st}, linearly to the perturbations of the reference Earth model according to

$$c_{st} = \int_0^a \delta m_{st}(r)\, K_s(r)\, \mathrm{d}r + \sum_d \delta h_{st}^d H_s^d, \qquad (1)$$

where $\delta m_{st}(r)$ are the coefficients of spherical harmonic expansions of angular order s and azimuthal order t for perturbations in *S*-wave

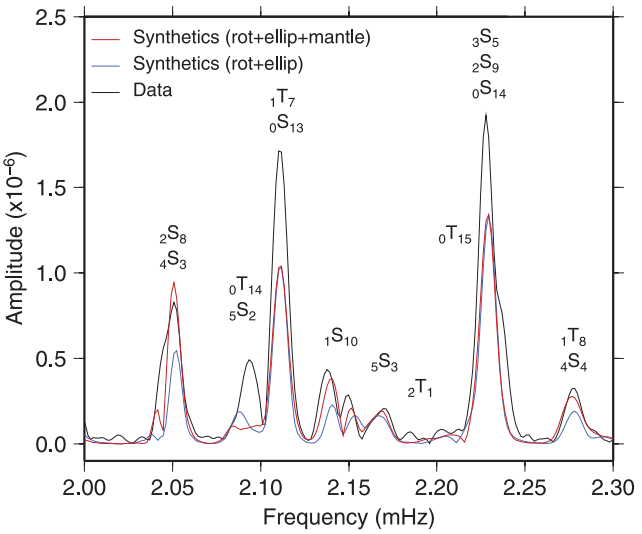

Figure 1. Amplitude spectrum of a Fourier transformed seismic record (5–70 hr) of the deep 1994 June 9 Bolivia earthquake recorded at station ATD (black) for a frequency window containing mantle sensitive modes. Synthetic data is calculated using full-coupling (Deuss & Woodhouse 2001) for rotation, ellipticity and heterogeneous mantle structure (red) and rotation and ellipticity only (blue). Theoretically predicted frequencies of normal modes are indicated.

velocity (V_s), *P*-wave velocity (V_p), density (ρ) and anisotropy. δh^d_{st} represent topography on discontinuities d and $K_s(r)$, H^d_s are the associated sensitivity kernels (Woodhouse 1980). All results in this study will be related to eq. (1) by considering the effect of variations in D″ structure (δm_{st} and δh_{st}) on the splitting of normal modes (c_{st}).

Splitting function maps $c(\theta, \phi)$ are used to visualize splitting functions. These plots are similar to phase velocity maps for surface waves and represent the local radial average of the underlying heterogeneity sampled by a particular mode below each point with colatitude θ and longitude ϕ according to

$$c(\theta, \phi) = \sum_{s=0}^{2l} \sum_{t=-s}^{s} c_{st} Y^t_s(\theta, \phi), \tag{2}$$

where $Y^t_s(\theta, \phi)$ are the complex spherical harmonics of Edmonds (1960) defined by

$$Y^t_s(\theta, \phi) = (-1)^t \left[\frac{(2s+1)(s-t)!}{4\pi (s+t)!} \right]^{\frac{1}{2}} P^t_s(\cos\theta) \, e^{it\phi}, \tag{3}$$

where P^t_s are the associated Legendre functions. The values of the splitting function $c(\theta, \phi)$ can be interpreted as the local variation from the degenerate frequency of the multiplet.

Some representative sensitivity kernels $K_s(r)$ ($s = 0$) for CMB sensitive normal modes are plotted in Fig. 2 showing a few general characteristics. The *S*-wave velocity kernels of the fundamental modes with $n = 0$ peak in the lowermost mantle for low angular order and they are sensitive to CMB topography (Fig. 2a) described by the kernels H^d_s. The fundamentals become progressively more sensitive to shallower structure for higher l (Figs 2b and c). The sensitivity to the D″ is shifted from the fundamental branch to the first overtone branch (Figs 2d–f) which turn into CMB Stoneley (interface confined) modes for l higher than 14. Modes of the third overtone branch are mainly sensitive to *S*-wave velocity and density (Fig. 2g) whereas fourth-order overtones also show strong *P*-wave velocity sensitivity (Figs 2h and i). Inner core sensitive modes such as ${}_3S_1$, ${}_{11}S_4$ and ${}_{13}S_1$ also show a significant sensitivity to CMB topography (Figs 2j–l).

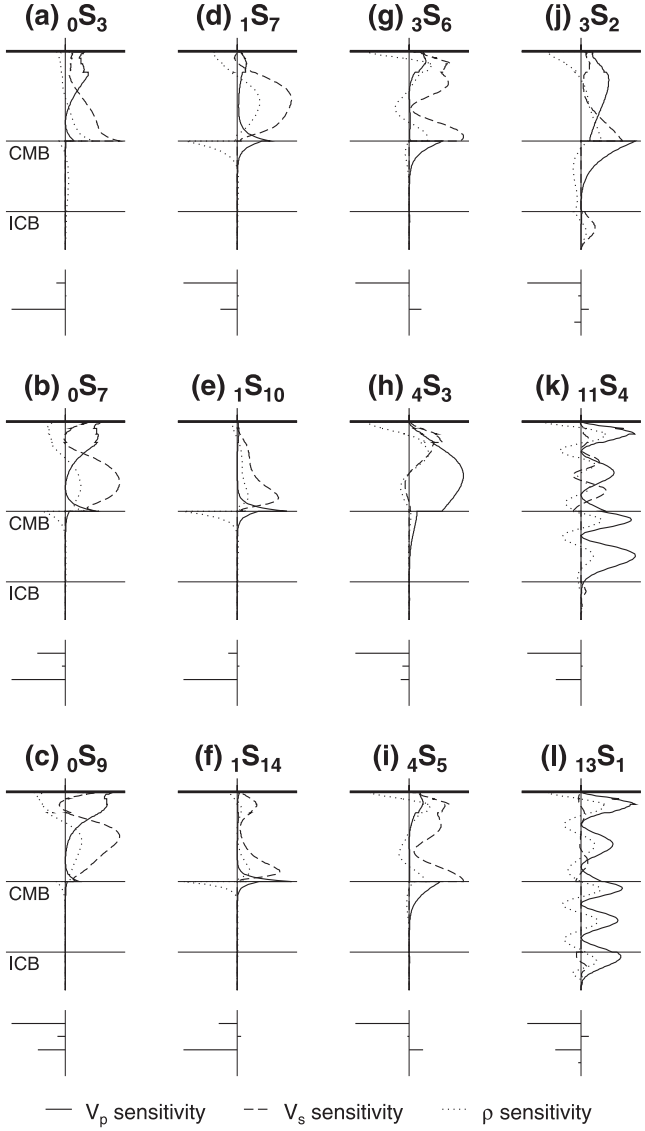

Figure 2. Sensitivity kernels (eq. 1) calculated using PREM for a range of CMB sensitive modes used in this study, showing sensitivity kernels $K_s(r)$ to *P*-wave velocity (solid), *S*-wave velocity (dashed) and density (dotted). The radii of the CMB and ICB are indicated by horizontal lines. The horizontal bars underneath the kernels show from top to bottom the mode's sensitivity (H^d_s) to topographic perturbations of the free surface, the 660 km discontinuity, CMB and ICB. Each graph is scaled independently.

3 METHODOLOGY

The occurrence of several large earthquakes in the last decade such as the Sumatra event of 2004, the Sichuan earthquake of 2008 and the Chile event of 2010, has provided a wealth of new data for observing normal modes. We make use of new splitting function data, which were obtained by inverting normal mode spectra from over 95 large earthquakes with $M_w > 7.6$ which occurred between 1976 and 2008 (Deuss *et al.* 2011). Splitting function data with corresponding uncertainties are shown in Fig. 3 for the c_{20} and Re(c_{22}) coefficients (eq. 1) for several normal modes listed in Table 1. Predictions for mantle and crust structure are calculated using 3-D mantle V_s model S20RTS (Ritsema *et al.* 1999) or S40RTS (Ritsema *et al.* 2011) and we correct for crustal thickness, surface topography and water level using model Crust5.1 (Mooney *et al.* 1998). We assumed scaling factors for *P*-wave velocity and density heterogeneities of the form $\delta \ln V_p / \delta \ln V_s = 0.5$ and $\delta \ln \rho / \delta \ln V_s = 0.3$ for S20RTS and a depth dependent linear scaling of $\delta \ln V_p / \delta \ln V_s =$ 0.5 (surface) to 0.33 (CMB) with $\delta \ln \rho / \delta \ln V_s = 0.3$ for S40RTS. This is consistent with previous work (Karato 1993; Ishii & Tromp 1999) and the development of the mantle models themselves; and within the ranges proposed by Li *et al.* (1991a). The observed splitting functions were already corrected for rotation and ellipticity, hence no correction is needed for the synthetic splitting functions.

The trends in the data are generally followed closely by splitting function predictions for these background models (Fig. 3). This implies that the additional splitting of normal modes due to small scale features in the D″ region will be obscured by these general trends, thereby complicating our investigation. It should be noted that the two coefficients depicted in Fig. 3 are the main contributors to the 'Ring around the Pacific' pattern observed in lowermost mantle tomography models (Ritsema *et al.* 2011).

Instead of calculating the splitting function coefficients according to eq. (1) for D″ features in addition to a background crustal and mantle model, we only compute the extra splitting caused by the small scale D″ structures in this sensitivity analysis. This forward modelling allows us to focus on small variations in the normal

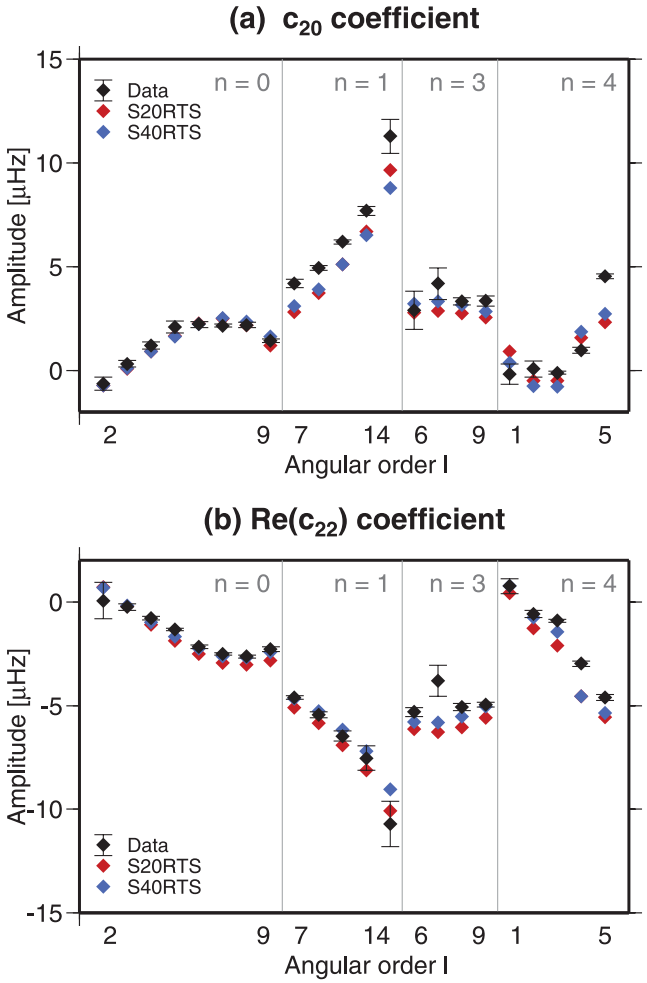

Figure 3. Splitting function coefficients in μHz (eq. 1) plotted for normal modes of the fundamental branch, first-, third- and fourth-order overtones for (a) the c_{20} coefficient and (b) the real part of the c_{22} coefficient. Values are plotted versus angular order l of each mode, which are grouped by radial order n as indicated by the separating vertical lines. Included modes are listed in Table 1. Data with error bars (black diamonds) are taken from Deuss *et al.* (2011) and values for mantle and crust structure are plotted with red and blue diamonds for S20RTS (Ritsema *et al.* 1999) and S40RTS (Ritsema *et al.* 2011) respectively, using Crust5.1 (Mooney *et al.* 1998) in both cases.

mode data. To give a quantitative measure whether these small variations in synthetic data are significant enough, we calculate the observability of inserted D″ structure according to

$$O_s = \frac{1}{2s+1} \sum_{t=-s}^{s} \frac{\left| c_{st}^{\text{structure}} \right|}{\sigma_{st}^{\text{data}}}, \tag{4}$$

where $c_{st}^{\text{structure}}$ is the predicted splitting function coefficient due to the D″ structure considered using eq. (1) and $\sigma_{st}^{\text{data}}$ is the uncertainty in the observed splitting function coefficient. The uncertainties in the data were estimated using the maximum spread in measured coefficients in cross-validation runs, where different events were left out in different runs (Deuss *et al.* 2011). O_s values larger than 1 imply that the effect of the inserted anomaly is larger than the uncertainty in the data and hence observable. For all the modes investigated in this study, we computed synthetic coefficients up to degree $s = 2l$ of the mode, up to a maximum of $s = 20$. We will focus here on O_2 as lowermost mantle models are dominated by a degree 2 pattern.

Table 1. List of lowermost mantle sensitive normal modes considered in this study. Inner core sensitive modes are indicated by an asterisk. The PREM frequency (f in mHz) and quality factor (Q) are given for each mode. We indicate for each mode whether the splitting functions have displayed significant variations, i.e., the O_2 values are larger than 1. T_p indicates whether O_2 is significant for differences in CMB topography patterns; T_a analogue for 5 km CMB topography amplitude in model LGW1991SAT. For ULVZs, U_r indicates whether O_2 is larger than 1 for regional ULVZs of 19 km thick and U_b shows whether banded ULVZs of 29 km are still observable. S indicates O_2 values larger than 1 for several $\delta \ln \rho / \delta \ln V_s$ ratios. Finally, for anisotropy, A_ϕ, A_ξ and A_η indicate whether 4 per cent anisotropy in a 150 km thick radial layer causes significant changes in O_2.

Mode	f	Q	T_p	T_a	U_r	U_b	S	A_ϕ	A_ξ	A_η
${}_0S_2$	0.31	510								
${}_0S_3$	0.47	418								
${}_0S_4$	0.65	373	x	x	x					
${}_0S_5$	0.84	356	x	x	x	x			x	
${}_0S_6$	1.04	347	x	x	x	x			x	
${}_0S_7$	1.23	342	x	x	x	x			x	
${}_0S_8$	1.41	337	x	x	x	x				
${}_0S_9$	1.58	333	x	x	x					
${}_1S_7$	1.66	372			x			x		
${}_1S_8$	1.80	379	x	x	x	x	x	x	x	
${}_1S_9$	1.96	380	x	x	x	x	x	x	x	
${}_1S_{10}$	2.15	378	x	x	x	x	x	x		
${}_1S_{14}$	2.98	293	x	x	x					
${}_2S_3*$	1.24	415			x	x		x		x
${}_3S_1*$	0.94	820	x	x	x			x		
${}_3S_2*$	1.11	367			x			x		x
${}_3S_6$	2.55	276			x	x		x		x
${}_3S_7$	2.69	269			x			x		x
${}_3S_8$	2.82	264	x	x	x	x	x	x		x
${}_3S_9$	2.95	259	x	x	x	x		x		x
${}_4S_1$	1.41	355								
${}_4S_2$	1.72	434								
${}_4S_3$	2.05	480			x		x		x	
${}_4S_4$	2.28	290	x	x	x	x		x		x
${}_4S_5$	2.41	282	x	x	x	x		x		x
${}_5S_3$	2.17	292	x	x	x	x		x	x	x
${}_5S_4$	2.38	489			x		x			
${}_5S_5$	2.70	503	x	x	x		x			
${}_5S_6$	3.01	506								
${}_5S_7$	3.29	493								
${}_5S_8$	3.53	418	x	x	x	x	x	x		x
${}_5S_{12}$	4.70	386			x	x		x		x
${}_7S_5$	3.66	477	x	x	x	x	x		x	x
${}_7S_6$	3.96	504	x	x	x		x		x	
${}_7S_7$	4.24	415	x	x			x	x		x
${}_8S_1*$	2.87	930						x		
${}_8S_7$	4.65	352	x	x	x	x		x		x
${}_{11}S_4*$	4.77	702	x	x						
${}_{11}S_5*$	5.07	666	x	x				x		x
${}_{12}S_8$	6.14	567			x	x	x			x
${}_{12}S_{12}$	7.46	570	x	x	x		x			x
${}_{13}S_1*$	4.50	735	x	x						
${}_{13}S_2*$	4.85	879	x	x			x	x		
${}_{13}S_3*$	5.19	909	x	x				x		
${}_{18}S_3*$	6.89	852	x					x		
${}_{18}S_4*$	7.24	943	x	x			x	x		
${}_{21}S_6*$	8.85	740	x							
${}_{21}S_7*$	9.17	800								
${}_{23}S_4*$	8.94	809	x	x				x		
${}_{23}S_5*$	9.29	899	x	x	x		x	x		

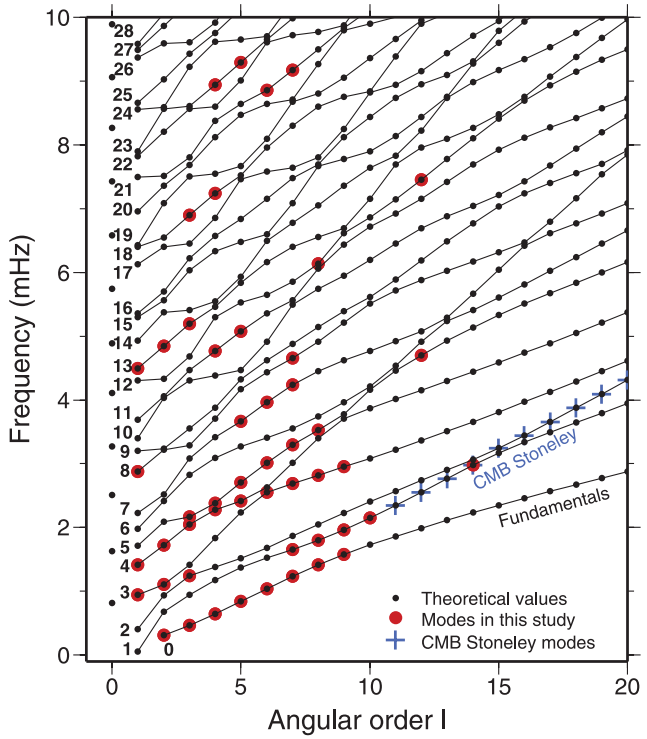

Figure 4. Dispersion diagram with theoretical frequencies of spheroidal modes (black) and CMB sensitive modes investigated in this study (red), plotted in the (frequency-*l*) plane. Lines joining dots define normal mode *branches* of constant radial order as indicated by their radial order *n*. The fundamental mode branch is indicated as well as the pseudo 'CMB Stoneley' branch (blue) corresponding to modes trapped on the CMB. This pseudo mode branch is made up of several segments of different mode branches, including ${}_1S_{11}$-${}_1S_{14}$, ${}_2S_{15}$-${}_2S_{25}$, ${}_3S_{26}$-${}_3S_{40}$, etc.

In the discussion (Section 6), we discuss higher degree observability. Our method of only considering the extra splitting to calculate the observability is justified as splitting function contributions can be linearly added according to eq. (1).

To use observability in a quantitative way to describe mode sensitivity, it is necessary to focus on modes for which the sensitivity kernels $K_s(r)$ peak in the D″ region or on modes with a strong sensitivity to CMB topography. Investigation of sensitivity kernels as those in Fig. 2 results in a subset of about 60 spheroidal modes which are indicated in Fig. 4 and listed in Table 1. Toroidal modes are excluded due their strong sensitivity to upper mantle anisotropy, which would complicate our analysis of the D″ substantially, and in addition due to fewer existing observations and their shallower sensitivity kernels. In the remainder of this study, we will use the subset of modes in Fig. 4 in observability histograms and present examples of individual observability values. We will use eq. (1) to calculate the splitting (c_{st}) of modes due to CMB topography, ULVZs, anisotropy and scaling between density and shear wave velocity heterogeneities. These lateral variations are defined relative to the radial reference model PREM (Dziewonski & Anderson 1981). In the sensitivity sections below, input models for these features are discussed more extensively.

In addition to showing observability values, splitting function maps (eq. 2) and individual splitting function coefficients (eq. 1) are presented for the discussion of trade-offs. These plots are useful for studying specific structural degrees of mantle heterogeneity and for identifying sensitive modes as sensitivity kernels vary smoothly along the dispersion branches (He & Tromp 1996). For these plots, D″ structure is included in addition to the background mantle model S20RTS (Ritsema *et al.* 1999) and crustal model Crust5.1 (Mooney *et al.* 1998) as discussed above.

4 MODE SENSITIVITY RESULTS

In all the results given below, we define the structure to be observable if the observability is larger than 1.

4.1 CMB topography

In the literature, many CMB topography models are found, obtained from seismic data, normal mode data, convection modelling or nutation data. We have experimented with a large number of these models and show here results for four different models: the normal mode model LGW1991SAT (Li *et al.* 1991b), the convection modelling derived model LMGZ2010PC1 (Lassak *et al.* 2010), the body wave model SV2003 (Sze & van der Hilst 2003) and the body wave model MD1987 (Morelli & Dziewonski 1987). The degree 2 component of these models, plotted in Fig. 5, shows that the pattern of the CMB topography in these models is quite different. We have also scaled the peak-to-peak amplitude of these topography models between 1 and 30 km to investigate the influence of the CMB topography amplitude.

In addition to calculating the observability values for these CMB topography models (e.g. the difference in splitting with and without topography on the CMB) according to eq. (4), we also calculate the difference in splitting between two CMB topography models with the same peak-to-peak amplitude using

$$\Delta_p(\text{model}) = \frac{1}{2s+1}\sum_{t=-s}^{s}\frac{\left|c_{st}^{\text{model}} - c_{st}^{\text{LGW1991SAT}}\right|}{\sigma_{st}^{\text{data}}}, \qquad (5)$$

where c_{st}^{model} and $c_{st}^{\text{LGW1991SAT}}$ are the predicted splitting function coefficients for a selected CMB topography model and the

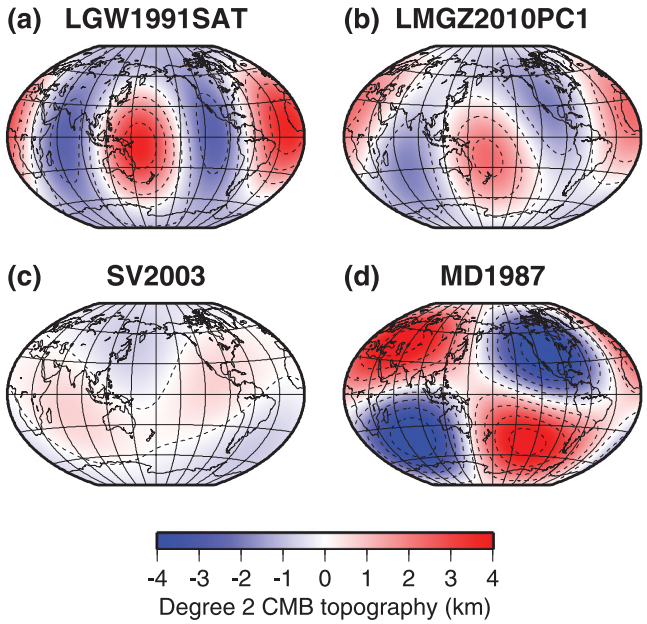

Figure 5. Long wavelength (degree 2) CMB topography for several existing models. (a) Normal mode model of Li *et al.* (1991b), (b) convection model of Lassak *et al.* (2010), (c) body wave model of Sze & van der Hilst (2003) and (d) body wave model of Morelli & Dziewonski (1987).

LGW1991SAT model, both scaled to peak-to-peak amplitudes of 5 km. Looking at the Δ_p values provides information as to whether the normal modes can distinguish between differences in CMB topography patterns.

4.1.1 Pattern of CMB topography

The degree 2 observability values for different CMB topography models are shown in Fig. 6(a) for a few example modes. The plot shows clearly how the sensitivity changes smoothly with angular order l. The observability values go up to 10 for some of these modes, with the fundamentals ($n = 0$) being affected significantly. These modes have the smallest uncertainties and have sensitivity to the CMB topography as shown in Figs 2(a)–(c). Including CMB topography alters the splitting of higher order overtones ($n = 3, 4$) depicted here to a lesser extent. Histograms of the observability for all the modes in Table 1 plotted for models LMGZ2010PC1 and SV2003 (Figs 6b and c) show that for convection model LMGZ2010PC1 the splitting is close to the limit of what can be observed with most values smaller than 1, whereas for the body wave model SV2003, about half of the values are larger than 1. Therefore, these CMB topography models lie at the limit of what normal modes can observe. Taking the difference between these topography models and the normal mode model LGW1991SAT (Figs 6d and e), however, suggests that differences between CMB topography patterns are observable with a reasonable number of modes displaying O_2 values larger than 1. In column T_p of Table 1, we have indicated for which modes the Δ_p values are larger than 1.

4.1.2 Amplitude of CMB topography

Fig. 7 presents the degree 2 observability values for model LGW1991SAT (Fig. 5a) scaled with peak-to-peak amplitudes of 1–30 km; the peak-to-peak CMB topography in the original model is 3.71 km. Again, we show individual values for some selected normal modes in Fig. 7(a) and histograms for all the modes of Table 1 (Figs 7b–e). The fundamental modes are split significantly by CMB topography, as well as the first order overtones and modes ${}_3S_8$, ${}_3S_9$, ${}_4S_4$ and ${}_4S_5$. Comparison of this figure with Fig. 6 illustrates that changing the amplitude of the CMB topography has a much more profound effect (about five times as large) on the normal modes than introducing a different pattern. Topographies of 1 km (Fig. 7b) are too small to be observed but topographies of 5 km cause splitting that is larger than the data uncertainty. In column T_a of Table 1, modes for which the observability values are larger than 1 for 5 km CMB topography are indicated by a cross. Scaling of the other CMB topography models of Fig. 5 gives rise to very similar, consistent results.

4.1.3 Inner core sensitive modes

Anomalous c_{20} coefficients for inner core sensitive modes, indicated in Table 1 with an asterisk, are usually explained as being due to inner core (IC) anisotropy (Woodhouse *et al.* 1986). In Fig. 8, we plot the c_{20} and Re(c_{22}) splitting function coefficients for a selection of these modes together with predictions for CMB topography models. For the Re(c_{22}) coefficient, mantle and crust predictions fit observations of inner core sensitive modes reasonably well. Inserting an increased CMB topography amplitude causes the predictions to deviate from the data. For the c_{20} coefficient, this is not the case and an increased amplitude seems to fit the data better. As inner core anisotropy is not included in our calculations, the predictions underpredict the observations. However, some of the anomalous c_{20} structure (though not all) could be due to CMB topography instead of anisotropy. In modelling IC anisotropy, CMB topography should therefore be taken into account as well.

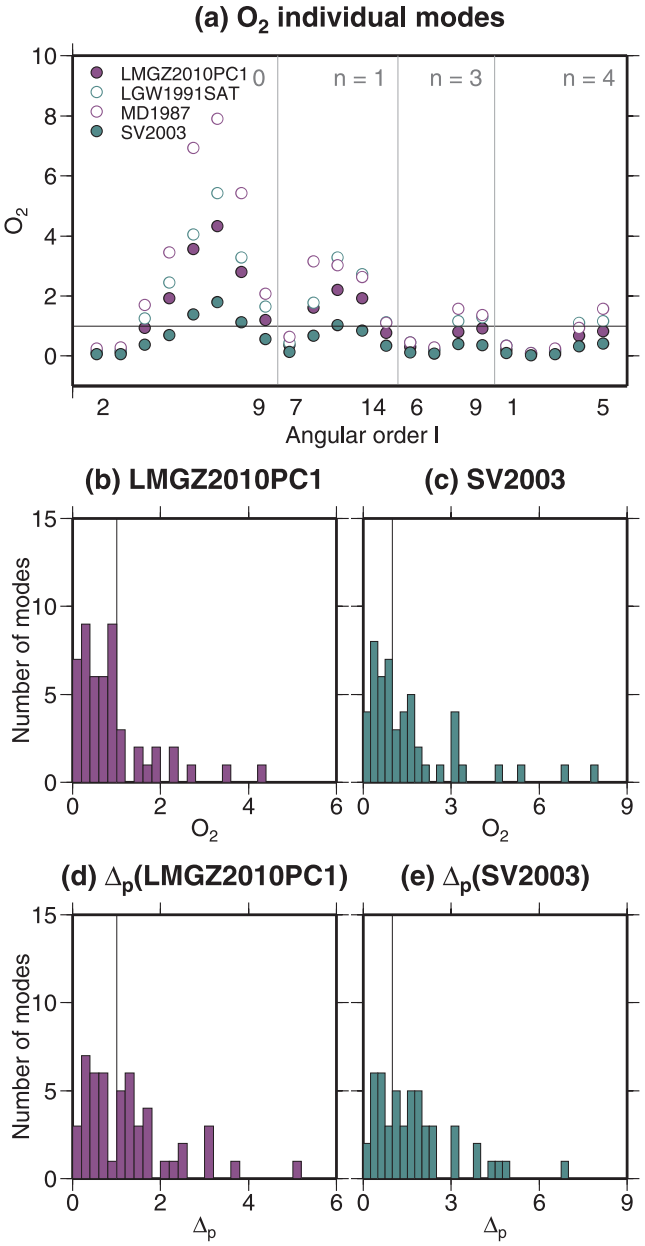

Figure 6. Degree 2 observability values (O_2) values plotted for lowermost mantle sensitive modes for different CMB topography models. (a) Some O_2 values are plotted for normal modes with simple sensitivity kernels ($n = 0$, 1, 3, 4) for CMB topography models LMGZ2010PC1 (filled purple), LGW1991SAT (open green), MD1987 (open purple) and SV2003 (filled green) similar to Fig. 3. The bottom panels show histograms of O_2 values for all the modes in Table 1 for (b) LMGZ2010PC1 and (c) SV2003, respectively, and Δ_p histograms for these models in (d) and (e), respectively. Values larger than 1 are significant as the splitting induced by the model is larger than the data uncertainty.

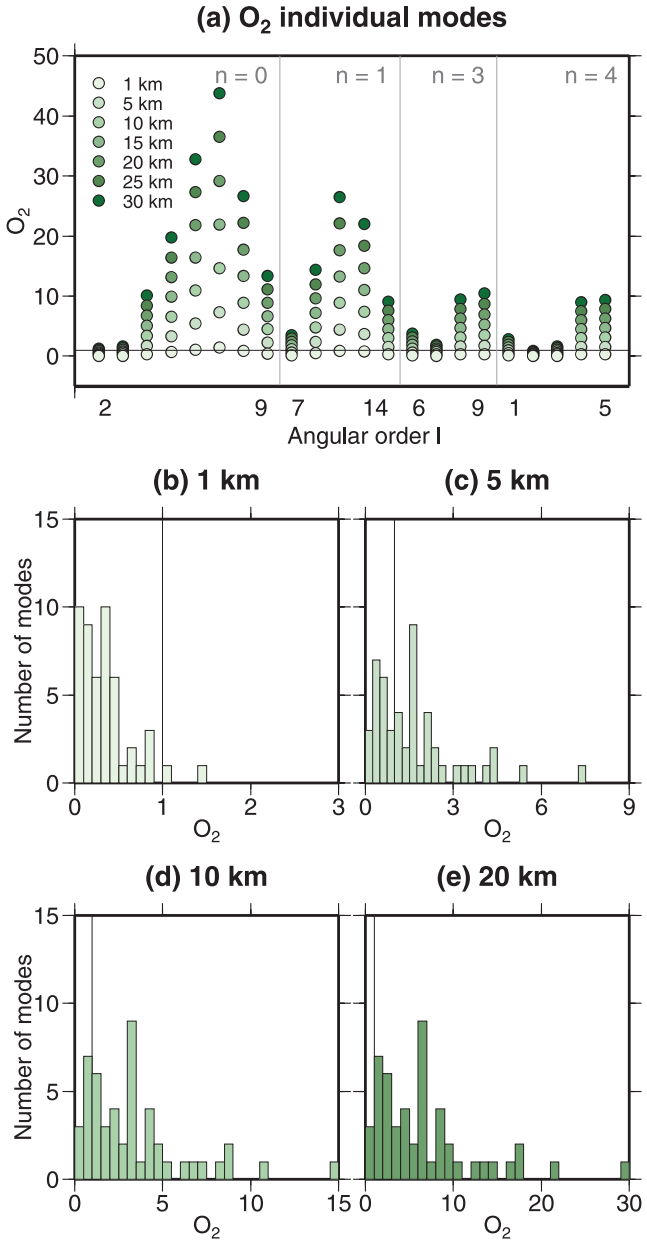

Figure 7. Similar to Fig. 6, O_2 values are plotted for lowermost mantle sensitive modes for CMB topography model LGW1991SAT with scaled amplitudes of 1 (light green), 5, 10, 15, 20, 25 and 30 (dark green) km. (a) Individual O_2 values are plotted for a few example modes. (b)–(e) show histograms of O_2 values for all modes in Table 1 for peak-to-peak amplitudes of 1, 5, 10 and 20 km. Note the difference in scale compared to Fig. 6.

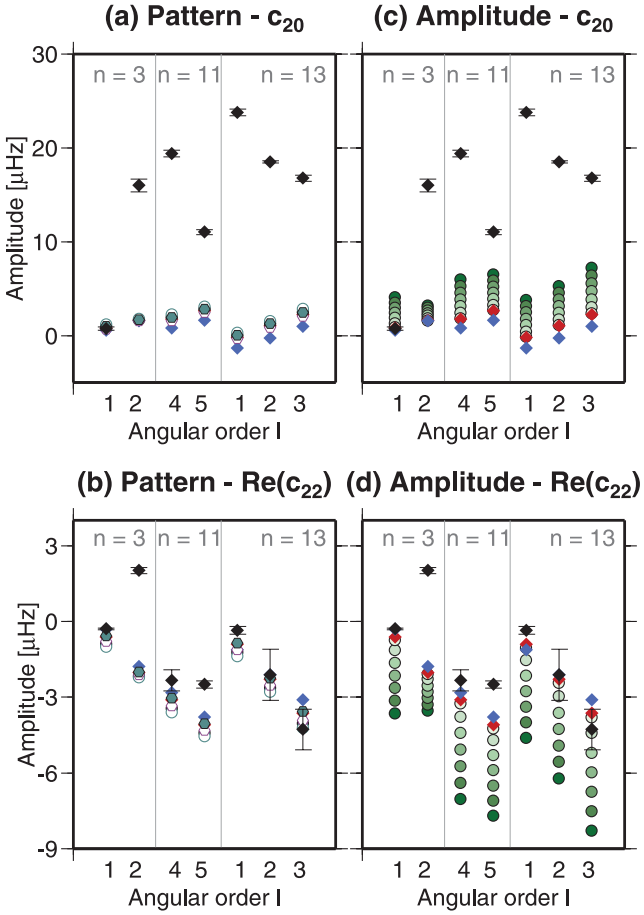

Figure 8. Splitting function coefficients as in Fig. 3 for inner core sensitive modes with predictions for (a and b) CMB topography patterns and (c and d) CMB topography amplitude added to the background mantle model. Symbols are as in Figs 6(a) and 7(a). Black, red and blue diamonds are used, respectively, for data (Deuss *et al.* 2011) and predictions for mantle and crust structure only using S20RTS (Ritsema *et al.* 1999) and S40RTS (Ritsema *et al.* 2011) with Crust5.1 (Mooney *et al.* 1998).

4.2 ULVZs

We study ULVZs in terms of their lateral extent and thickness. These features have never been studied with normal modes before. We particularly investigate what the limits are in distinguishing possible ULVZs in the normal mode data as these features might be so thin that they are not observable at all. Variations are taken as -30, -10 and $+10$ per cent for $\mathrm{d}\ln V_s$, $\mathrm{d}\ln V_p$ and $\mathrm{d}\ln\rho$, respectively, and we vary the thickness between 2 and 47 km, consistent with previous work (Thorne & Garnero 2004; Garnero & McNamara 2008). In terms of distribution, we insert three different ULVZ distributions based on the S20RTS velocity distribution in the deep mantle (Fig. 9a). The distribution of ULVZ material is either global (where $\mathrm{d}\ln V_s < 0$ per cent in S20RTS as in Fig. 9b), regional (where $\mathrm{d}\ln V_s < -0.5$ per cent in S20RTS Fig. 9c) or confined to bands for $-0.8 < \mathrm{d}\ln V_s < -0.5$ per cent in S20RTS (Fig. 9d). The global and regional distributions resemble the occurrence of LLSVPs (Garnero & McNamara 2008) and the banded ULVZ distribution correspond to the edges of the LLSVPs where ULVZs are dynamically thought to occur (McNamara *et al.* 2010). Although these distributions are more organised than the observed patchy distribution of ULVZs, these models still allow us to identify which modes respond to ULVZ signals.

Fig. 10 shows the degree 2 observability values for the different ULVZ distributions. The effect of global ULVZs is substantial (Fig. 10a), similar to inserting large CMB topographies (Fig. 7a). Even ULVZs as thin as 2 km give O_2 values larger than 1 for modes such as ${}_0S_7$, ${}_1S_9$ and ${}_4S_4$. For regional ULVZs (Fig. 10b), the values are very similar even though the lateral extent of the ULVZ material is reduced significantly (compare Figs 9b and c) suggesting that the ULVZ thickness is more important than its lateral extent. For more realistic distributions of banded ULVZs (Fig. 10c) the observability values are substantially lower (note the difference in axis). However, for ULVZ thicknesses larger than 19 km, the values are still notably larger than 1 for a number of modes. For this selection of modes, the effect of ULVZs is strongest for fourth-order overtones ($n = 4$)

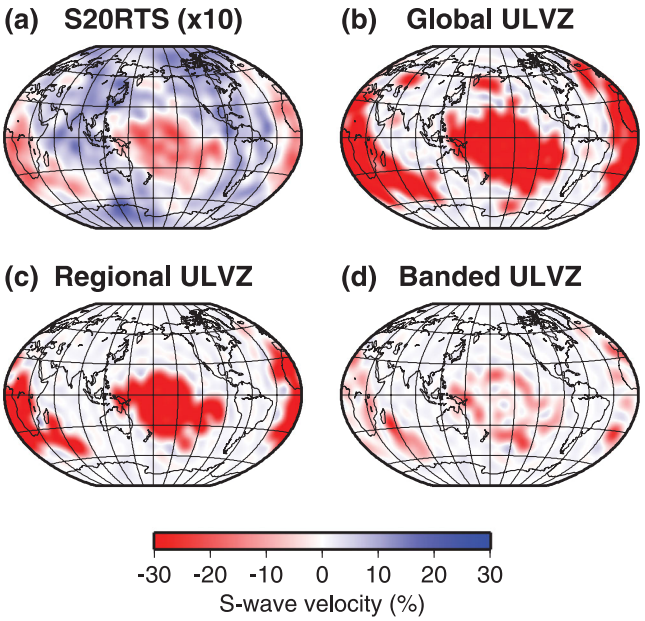

Figure 9. *S*-wave velocity at the CMB for (a) the background model S20RTS (×10), (b) global ULVZs, (c) regional ULVZs and (d) banded ULVZs, all with a 30 per cent reduction in *S*-wave velocity. The ULVZs are parametrized in terms of the *S*-wave velocity variations in S20RTS as discussed in the text. *P*-wave velocity and density are computed analogue with a 10 per cent reduction and 10 per cent increase, respectively.

which showed no sensitivity to CMB topography (Fig. 7a). Every branch depicted here seems to contain some modes with sensitivity to ULVZs, including the fundamentals.

Fig. 10 merely served to show examples of how the observability changes along the normal mode branches and how sensitive normal modes can be identified. In Fig. 11, we plot histograms of the degree 2 observability of all modes in Table 1 to regional and banded ULVZs. These plots show that for 2 km thick regional ULVZs mainly have O_2 values smaller than 1 and hence cannot be observed. On the other hand, splitting due to regional ULVZs with thicknesses larger 19 km is significant enough to be observable. Banded ULVZs have to be at least 29 km thick unless they cannot be observed realistically. However, it is interesting that ULVZs of 19 km thick already show a significant effect on splitting of normal modes, so layers much thinner than 100 km can be identified in normal mode data. In Table 1, we indicate which modes show significant splitting for regional ULVZs of 19 km thick (U_r) and for banded ULVZs of 29 km thick (U_b).

Comparing the observability values for ULVZs to CMB topography, we find that the effect of regional ULVZs is of similar amplitude as large peak-to-peak CMB topography amplitudes and significantly larger than different CMB topography patterns. The effect of banded ULVZs is comparable in magnitude to the effect of different CMB topography models. Some modes respond more strongly to CMB topography than ULVZs and vice verse, as expected from their sensitivity kernels. The possible trade-offs between these features will be discussed in more detail in Section 5.

One might argue that for studying ULVZs, higher structural degrees are more important to study. However, our current ULVZ input models all have a very strong degree 2 component, even for banded ULVZ distributions. This long wavelength component could be viable if ULVZs dynamically occur on the edges of LLSVPs (McNamara *et al.* 2010). In addition, for higher structural degrees, the absolute amplitude of the coefficients is smaller and the corresponding uncertainties in the data are larger. Also, the amplitude spectrum of banded ULVZs only deviates from that of regional ULVZs for structural degrees higher than 18 for which no normal mode data is available at present.

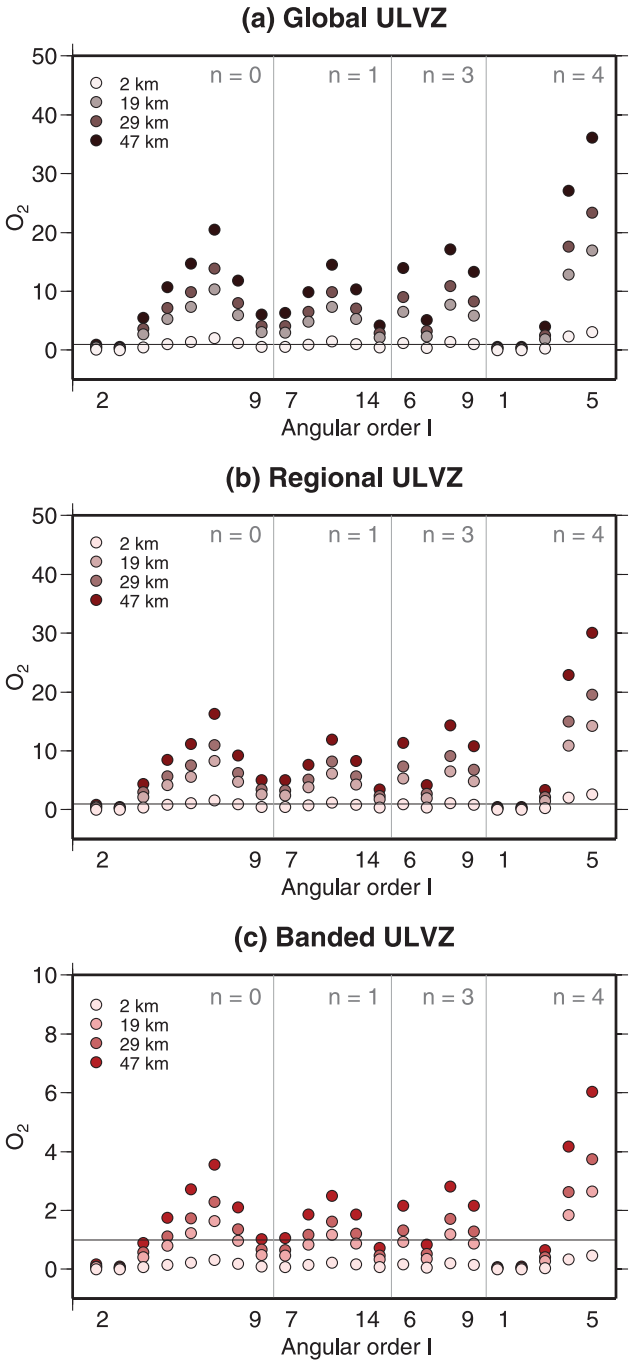

Figure 10. O_2 values plotted for lowermost mantle sensitive modes similar to Fig. 6 for different ULVZ distributions with in (a) global ULVZs, (b) regional ULVZs and (c) banded ULVZs as specified in Fig. 9. Values are plotted for ULVZs of 2 (light), 19, 29 and 47 (dark) km thick. Note the difference in scale between the panels. O_2 values larger than 1 are significant.

4.3 $\delta \ln \rho / \delta \ln V_s$ scaling

Anticorrelation in D″ is parametrized by scaling *P*-wave velocity and density heterogeneities to *S*-wave velocity heterogeneities in

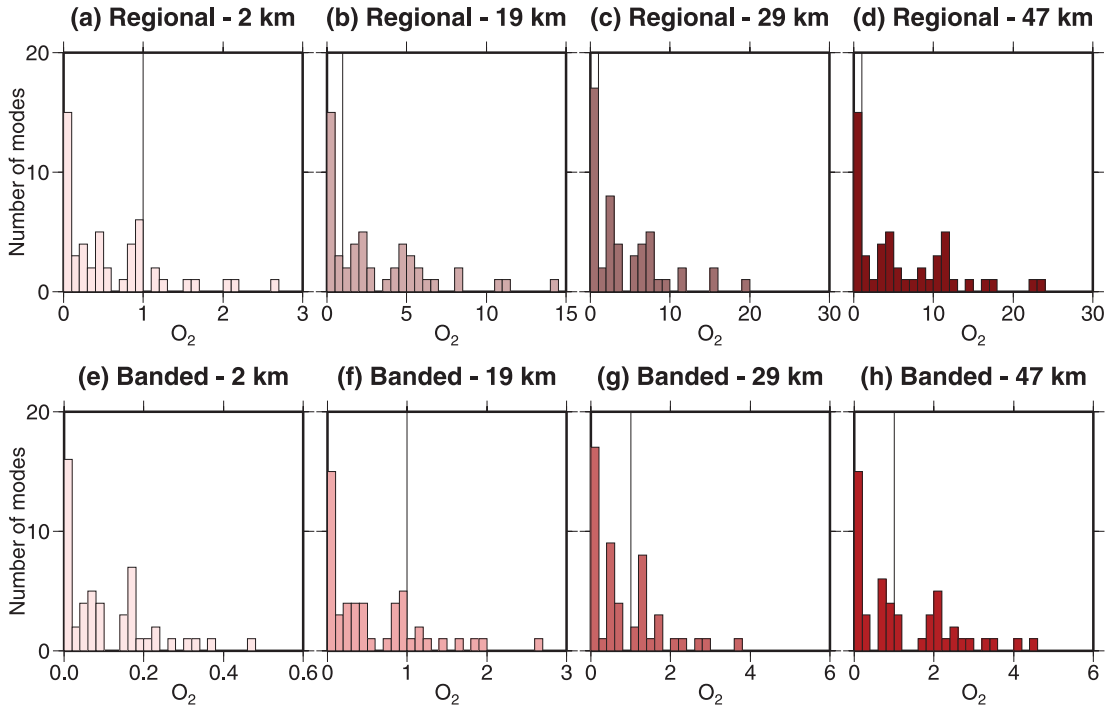

Figure 11. Histograms of O_2 values for all modes in Table 1 for regional (a–d) and banded (e–h) ULVZs with thicknesses of 2 km (a,e), 19 km (b,f), 29 km (c,g) and 47 km (d,h). Note the difference in horizontal axis between the different panels. The colours correspond to the symbols in Fig. 10.

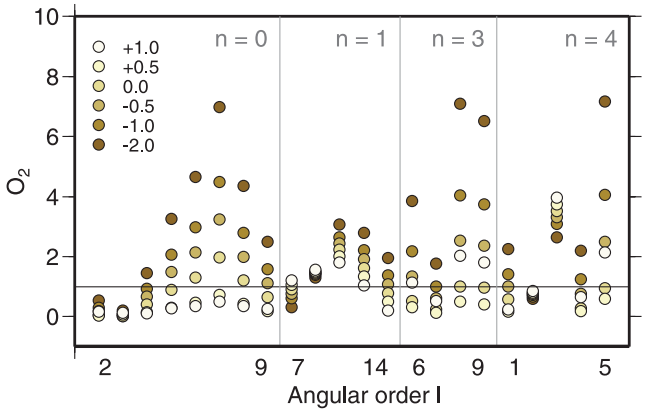

Figure 12. Degree 2 observability values plotted for modes of the fundamental, first-, third- and fourth-order overtones for varying radial $\delta\ln\rho/\delta\ln V_s$ scaling of +1 (white), 0.5, 0.0, −0.5, −1.0 and −2.0 (gold) in a 315 km thick layer with $\delta\ln V_p/\delta\ln V_s = 0.2$.

mantle model S20RTS. The input structures of the *P*-wave velocity and density perturbations are thus exact scaled versions of the *S*-wave velocity model, similar to that shown in Fig. 9(a). In this study, $\delta\ln V_p/\delta\ln V_s$ is set to 0.2 and $\delta\ln\rho/\delta\ln V_s$ is changed from 0.3 to values between +1 and −2 in a radial layer of 75, 150, 225 and 315 km thick above the CMB. This anticorrelation is mainly included here to study whether $\delta\ln\rho/\delta\ln V_s$ scaling can induce trade-offs in such a way that larger CMB topography or thicker ULVZs would be allowed.

Fig. 12 shows the observability values of the normal modes due to a varying $\delta\ln\rho/\delta\ln V_s$ ratio in a 315 km thick layer above the CMB. For most of the normal mode examples shown in this figure, different ratio values gives rise to significant splitting with O_2 values larger than 1. This plot shows a more complicated behaviour for the observability values than just a simple increase or decrease in O_2 values, complicating any inferences that might be drawn. However, there is a number of modes with $O_2 > 1$ for different $\delta\ln\rho/\delta\ln V_s$ scaling factors, as indicated in column *S* of Table 1.

The influence of the thickness of the $\delta\ln\rho/\delta\ln V_s$ scaling layer is relatively small and the $\delta\ln V_p/\delta\ln V_s$ ratio also only has a minor influence. Changing the $\delta\ln\rho/\delta\ln V_s$ ratio has a more profound effect than either of these, so it is possible to constrain this ratio reasonable accurately in tomographical inversions even if different layer thicknesses are assumed. The O_2 values are comparable in amplitude to those for different CMB topography patterns and banded ULVZs but smaller than the effect of regional ULVZs and CMB topography amplitude.

The complex pattern observed in Fig. 12 in combination with the suggestion of chemical heterogeneity in the deep mantle (Deschamps *et al.* 2007; Garnero & McNamara 2008; McNamara *et al.* 2010; Lay & Garnero 2011) suggests the existence of a laterally varying ratio between density and *S*-wave velocity perturbations in the lowermost mantle. Indeed, for a number of modes, predictions for the c_{20} coefficient match the observations best for a positive $\delta\ln\rho/\delta\ln V_s$ ratio whereas the data for the Re(c_{22}) coefficient seem to favour a more negative ratio. This is seen for thick layers of 315 km as well as for thinner deeper layers suggesting that the signal of variable $\delta\ln\rho/\delta\ln V_s$ ratio originates in the lowermost mantle.

A simple forward modelling test is performed to investigate what a possible pattern for the laterally varying $\delta\ln\rho/\delta\ln V_s$ ratio could be. We calculate L1 misfit values between the observed and predicted degree 2 splitting function coefficients for different $\delta\ln\rho/\delta\ln V_s$ ratios. For each degree 2 coefficient, we pick the value of the ratio with the lowest misfit. We use the uncertainties in the data to normalize the misfit and only include the modes for which we demonstrated that they are sensitive to the different ratios (Table 1). We subsequently plot the resulting laterally varying pattern of the $\delta\ln\rho/\delta\ln V_s$ ratio. The result of this simple forward calculation test is shown in

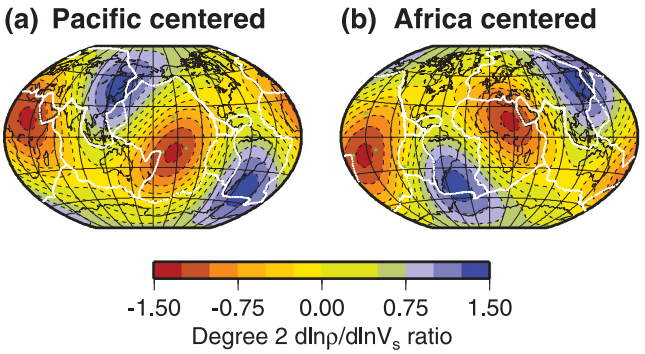

Figure 13. Degree 2 pattern [Pacific (left) and Africa (right) view] of the $\delta\ln\rho/\delta\ln V_s$ ratio obtained from a simple test using only modes with O_2 values larger than 1. The pattern shows a negative ratio under the southwest Pacific and Central Africa, more or less consistent with the locations of the LLSVPs and the results of Ishii & Tromp (1999) and Trampert *et al.* (2004).

Fig. 13. The pattern shows weak positive $\delta\ln\rho/\delta\ln V_s$ ratios underneath the locations of subduction zones and a negative $\delta\ln\rho/\delta\ln V_s$ ratio for LLSVP locations. Mineral physics estimates of this ratio for purely thermal variations lie between 0.2 and 0.4 (Anderson 1987, 1989). The normal mode data is, therefore, consistent with a thermal origin for velocity anomalies beneath the Pacific rim, whereas the ratios at the location of LLSVPs suggest a chemical origin consistent with previous work (Ishii & Tromp 1999; Trampert *et al.* 2004).

4.4 Anisotropy

Anisotropy is parametrized assuming transverse vertical isotropy. In this case, the lateral heterogeneities in seismic velocities can be described in terms of the Love parameters A, C, L, N and F (Love 1927). These are related to the horizontally and vertically polarized seismic velocities by $V_{ph} = \sqrt{A/\rho}$, $V_{pv} = \sqrt{C/\rho}$, $V_{sh} = \sqrt{N/\rho}$, $V_{sv} = \sqrt{L/\rho}$, giving rise to the anisotropy parameters $\xi = N/L$ (S-wave velocity anisotropy), $\phi = C/A$ (P-wave velocity anisotropy) and $\eta = F/(A - 2L)$ for anisotropy in the incident angle. In an isotropic earth model, these parameters are equal to 1. Sensitivity kernels K_ϕ, K_ξ and K_η for these parameters are derived following Dahlen & Tromp (1998) resulting in

$$K_\phi = AK_C, \tag{6}$$

$$K_\xi = LK_N, \tag{7}$$

$$K_\eta = (A - 2L)K_F, \tag{8}$$

where K_C, K_N and K_F are the kernels corresponding to variations in the Love parameters C, N and F (Dahlen & Tromp 1998). Examples of these kernels are given in Fig. 14.

The influence of the individual anisotropy parameters is investigated by inserting a laterally varying anisotropic layer of 150 km atop the CMB with variations of up to 10 per cent (e.g. $0.9 < \phi, \xi, \eta < 1.1$) as depicted in Fig. 15. These values are comparable with the range of anisotropy in the upper mantle (Dziewonski & Anderson 1981; Montagner & Kennett 1996). We relate the anisotropy perturbations to the S-wave velocity perturbations in S20RTS (Fig. 15). Negative (positive) values are assumed where negative (positive) S-wave velocity perturbations occur in S20RTS. S waves have a higher velocity parallel to the CMB for ξ-values greater than 1.0 ($V_{sh} > V_{sv}$) and in regions where ξ is less than 1.0 the S waves

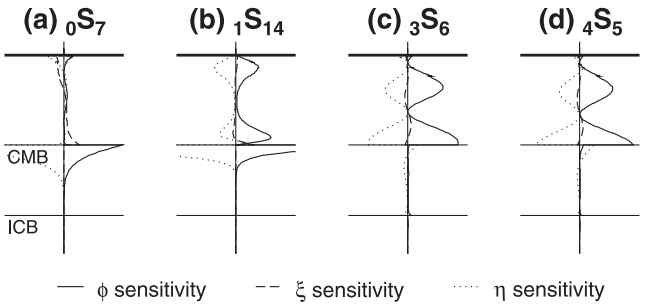

Figure 14. Sensitivity kernels calculated using PREM for some CMB sensitive modes used in this study: (a) $_0S_7$, (b) $_1S_{10}$, (c) $_3S_8$ and (d) $_4S_5$ showing sensitivity to ϕ (solid), ξ (dashed) and η (dotted). The radii of the CMB and ICB are indicated by horizontal lines. Note that the horizontal scale is the same for all panels.

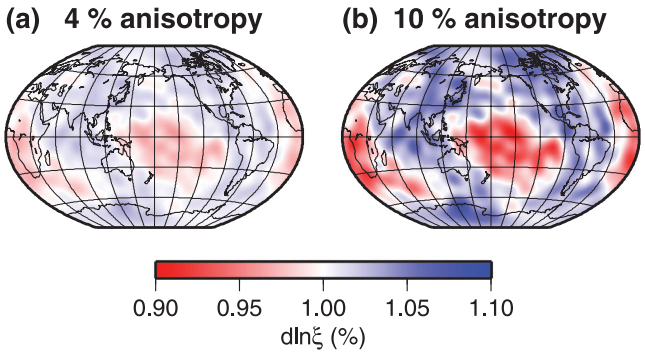

Figure 15. Examples of laterally varying input models for S-wave velocity anisotropy (ξ). $V_{\rm sh}$ is larger than $V_{\rm sv}$ in regions where ξ is larger than 1 whereas $V_{\rm sv}$ is larger than $V_{\rm sh}$ if ξ is less than 1.

are faster perpendicular to the CMB ($V_{sv} > V_{sh}$). This results in an overall degree 2 pattern, consistent with the anisotropy model of Panning & Romanowicz (2006). Other anisotropy parameters are scaled in an analogue way.

Degree 2 observability values are plotted in Fig. 16 for a selection of lowermost mantle sensitive modes for the different anisotropy parameters that have been varied individually. The fundamental modes ($n = 0$) show no sensitivity to ϕ and η but are able to observe variations in ξ whereas the first-order overtones ($n = 1$) are moderately sensitive to all three anisotropy parameters. The third- and fourth-order overtones ($n = 3, 4$) on the other hand display a strong sensitivity to anisotropy in both ϕ and η. These findings match the behaviour seen in the sensitivity kernels in Fig. 14. For all parameters, anisotropy of 2 per cent is generally too small to be observable with only a few modes having values larger than 1. In Table 1, modes with O_2 values larger than 1 for 4 per cent anisotropy in either ϕ, ξ or η are indicated, showing that most modes are sensitive to P-wave velocity anisotropy.

In Fig. 16, we see that modes that are sensitive to anisotropy in P-wave velocity (ϕ) are also sensitive to anisotropy in the incident angle (η). This could be an indication of possible trade-offs between ϕ and η, especially for the third- ($n = 3$) and fourth- ($n = 4$) order overtones. Therefore, in Fig. 17 we plot the splitting function predictions for the c_{20} coefficient for observed and predicted coefficients for anisotropy in these two parameters. For the fundamentals and first-order overtones, adding anisotropy has the same effect on the splitting function coefficients for both parameters. However, for the third-and fourth-order overtones, introducing P-wave velocity anisotropy (ϕ) or anisotropy in η have a strong opposite effects,

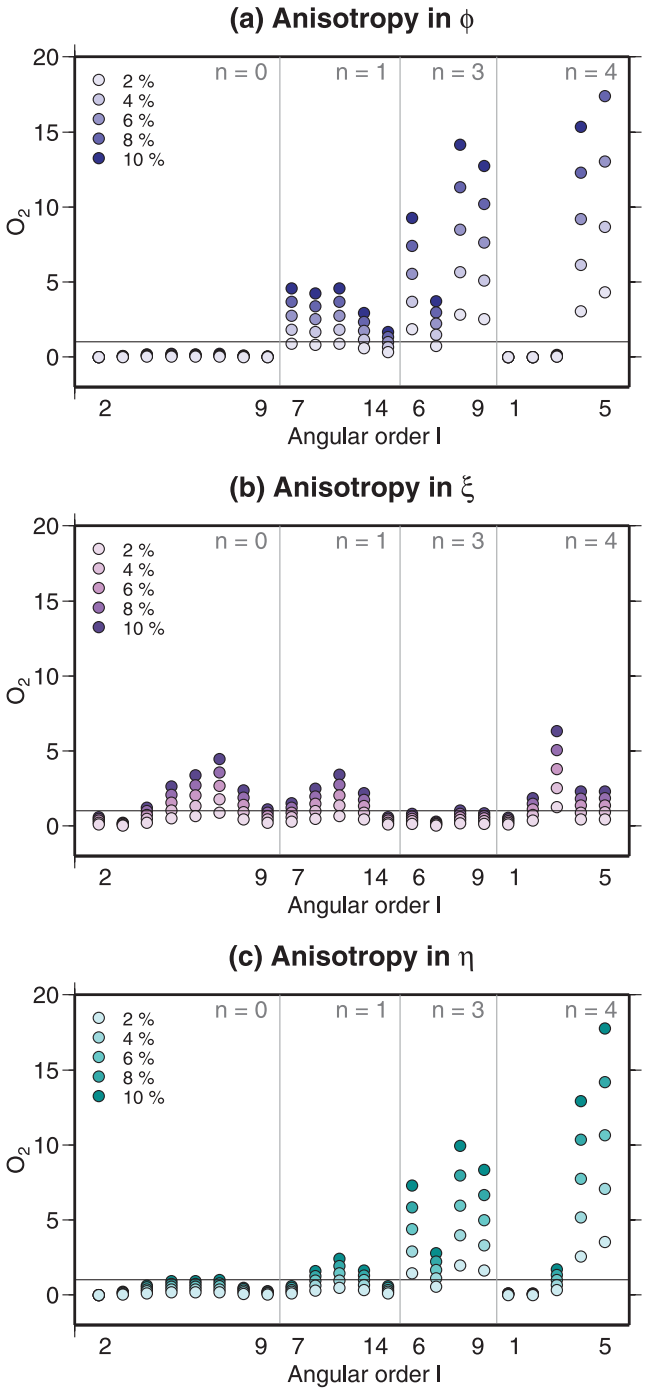

Figure 16. O_2 values plotted for lowermost mantle sensitive modes for laterally varying anisotropy for (a) anisotropy in ϕ, (b) anisotropy in ξ and (c) anisotropy in η. Anisotropy parameters are varied individually in steps of 2 per cent up to a maximum value of 10 per cent according to the pattern plotted in Fig. 15.

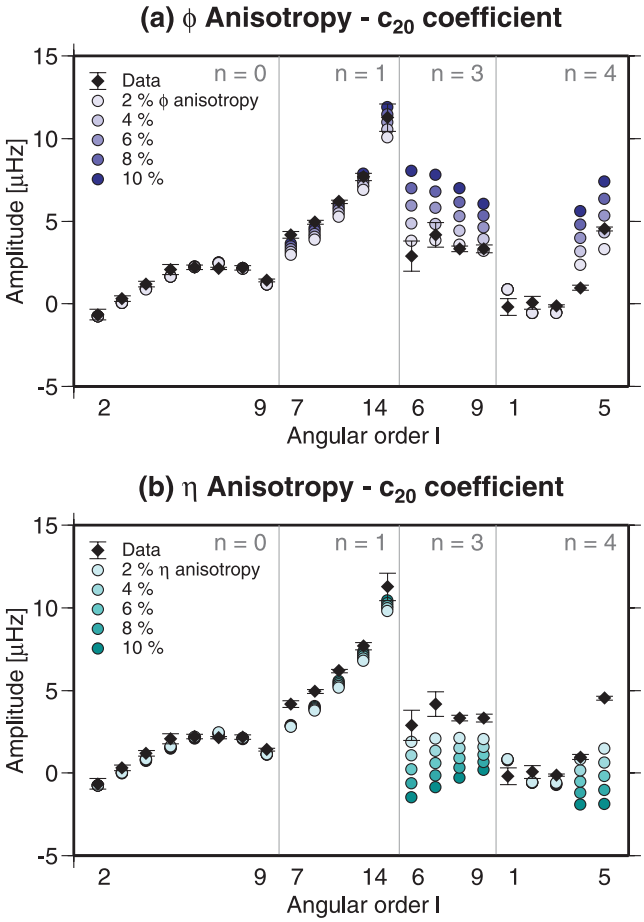

Figure 17. c_{20} splitting function coefficients in μHz for laterally varying anisotropy for (a) anisotropy in ϕ and (b) anisotropy in η. Predictions are computed for S20RTS with additional anisotropy in a layer of 150-km-thick atop the CMB and compared with observed coefficients (black) Deuss *et al.* (2011). The pattern of anisotropy is shown in Fig. 15 and the magnitude is varied in steps of 2 per cent up to a maximum value of 10 per cent (dark).

giving rise to a trade-off between these two parameters. This is observed for modes of the eighth-order overtone branch ($n = 8$) as well. Fortunately, there are also normal modes that only show sensitivity to either ϕ or η as is demonstrated in Table 1. Constraining anisotropy in the lowermost mantle will be complicated by this trade-off and the overall small sensitivity to S-wave velocity anisotropy (ξ).

5 TRADE-OFFS BETWEEN D″ STRUCTURES

We have demonstrated in the previous section how strongly anomalous structures in the D″ region and topography on the CMB have to be to be observable in normal mode data. We have shortly compared the effect of the various structures, but the question remains what trade-offs exist between these different features. The main sensitivities are summarized in Table 1 which can be used as a reference for future normal mode studies of the lowermost mantle. To illustrate the relative importance and to discuss the possible trade-offs between D″ structures, we show in Fig. 18 splitting function predictions for the c_{20} coefficient for input models of CMB topography, ULVZs, $\delta\ln\rho/\delta\ln V_s$ ratios and anisotropy in P-wave velocity. The predictions for mantle structure of S20RTS and S40RTS only are not plotted in this figure but follow the observations closely as is observed in Fig. 3(a).

For the fundamental modes ($n = 0$), CMB topography and ULVZs have the largest effect on the splitting functions. These two features reinforce each other, excluding the possibility of a trade-off between the two. Similar patterns are observed for the first-order overtones ($n = 1$), although for modes with high angular order ($l = 10$, 14), the effect of $\delta\ln\rho/\delta\ln V_s$ scaling becomes more significant. Even though the $\delta\ln\rho/\delta\ln V_s$ scaling trade-offs with CMB topography and

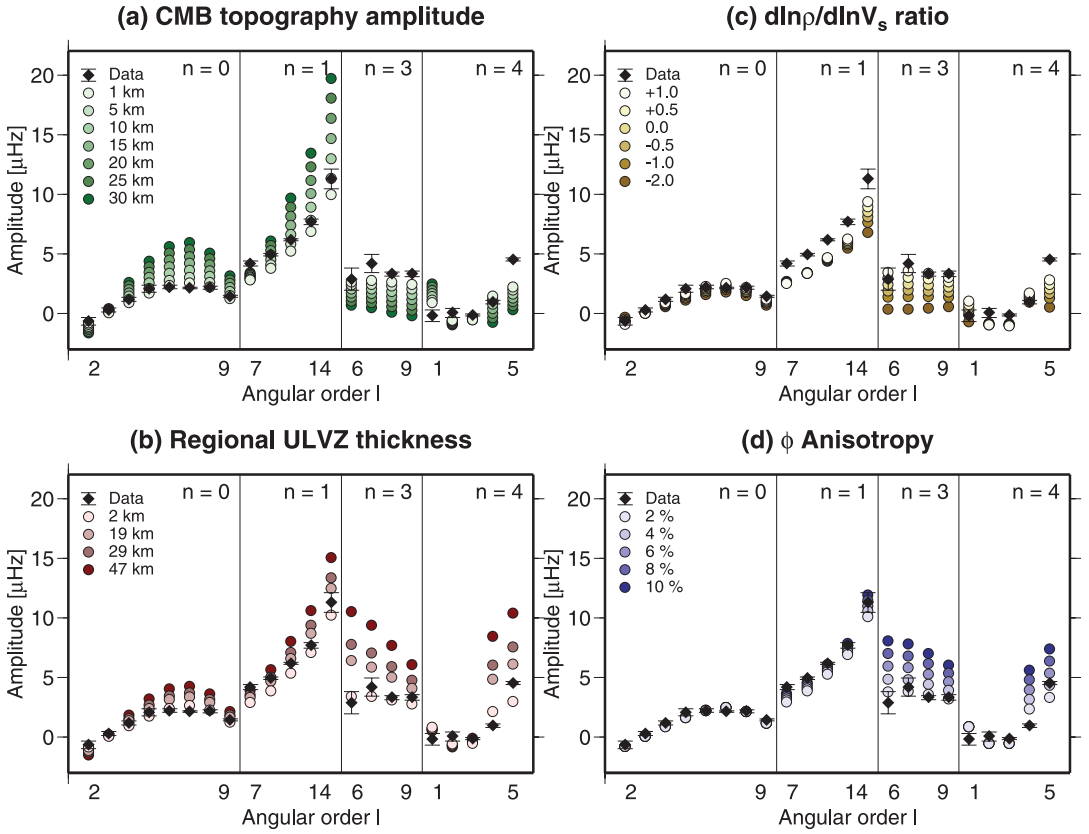

Figure 18. c_{20} splitting function coefficient predictions in μHz for lowermost mantle structures for modes of the fundamental, first-, third- and fourth-order overtones. (a) Predictions for the CMB topography model LGW1991SAT with scaled amplitude, (b) predictions for regional ULVZs with different thicknesses, (c) predictions for different $\delta\ln\rho/\delta\ln V_s$ ratios and (d) predictions for laterally varying anisotropy in *P*-wave velocity. All other symbols are as in Fig. 3. Note the constant vertical scale for convenience of identifying trade-offs.

ULVZs for these modes, the effect is still significantly smaller. Even for an extreme $\delta\ln\rho/\delta\ln V_s$ ratio of -2, only a peak-to-peak CMB topography of 10 km is compatible with the data. For the third-order overtones, all investigated features have a profound effect and trade-offs exist in various ways; between CMB topography and ULVZs, between CMB topography and *P*-wave velocity anisotropy, between $\delta\ln\rho/\delta\ln V_s$ scaling and anisotropy, etc. This is complicated further by the trade-offs between anisotropy in ϕ and η (Fig. 17). Similarly, for the fourth-order overtones, all D$''$ structures influence the splitting functions leading to several trade-offs, although for ${}_4S_1$, only CMB topography and $\delta\ln\rho/\delta\ln V_s$ scaling is of influence.

Thus, we find that multiple trade-offs exist between the different lowermost mantle structures in normal mode data. It should be pointed out though, that the modes shown in this figure (Fig. 18) are merely an example of all the modes currently observed and a significantly larger number of modes has sensitivity to the lowermost mantle. Trade-offs are very dependent on the normal mode considered. Some of these modes only display significant sensitivity to one particular feature, such as ${}_0S_4$ to CMB topography or ${}_5S_6$ to $\delta\ln\rho/\delta\ln V_s$ scaling. In addition, certain branches may display a trade-off between $\delta\ln\rho/\delta\ln V_s$ scaling and ULVZs (such as the third-order overtone branch), whereas other branches show no trade-off between those features (e.g. eighth-order overtones). The fundamental and first-order overtones are mainly sensitive to CMB topography and ULVZs and can, hence, be used to constrain these accurately, providing information that can be used to resolve trade-offs in other overtones. By combining all normal mode branches with different sensitivities and trade-offs together, it is, therefore, still possible to deduce valuable information regarding structures in Earth's lowermost mantle.

The discussion of trade-offs above is based on the splitting function predictions for the c_{20} coefficient. To demonstrate that the identified trade-offs are independent of the splitting function coefficient considered, we plot in Fig. 19 splitting function maps for ${}_1S_{14}$. Corresponding sensitivity kernels are given in Figs 2(f) and 14(b). Fig. 19 gives the observed splitting function and predictions for CMB topography, ULVZs, anticorrelation and anisotropy. Splitting functions for angular order 2 are computed for realistic (left-hand side panels) and more extreme structure (right-hand side panels). All maps show a strong 'Ring around the Pacific' pattern, consistent with the overall dominant pattern in the lowermost mantle (Deuss *et al.* 2011). The predicted splitting function for mantle and crust structure only (Fig. 19b) resembles the observed splitting function (Fig. 19a) well but underestimates the extrema slightly.

Adding realistic D$''$ structure to the mantle model (left-hand side panels) illustrates the small influence of these features on the splitting function. The predictions resemble the observation well and only the addition of 10 km CMB topography (Fig. 19c) has a significant effect. Adding more extreme structures (right-hand side panels) shows that the splitting function predictions are affected more severely. In some cases, the splitting function amplitude becomes unrealistically large, especially when large CMB topography (Fig. 19d) or regional ULVZs are inserted (Fig. 19h). As we have only performed forward calculations, we cannot exclude any of these structures as possibility for the lowermost mantle. However, the

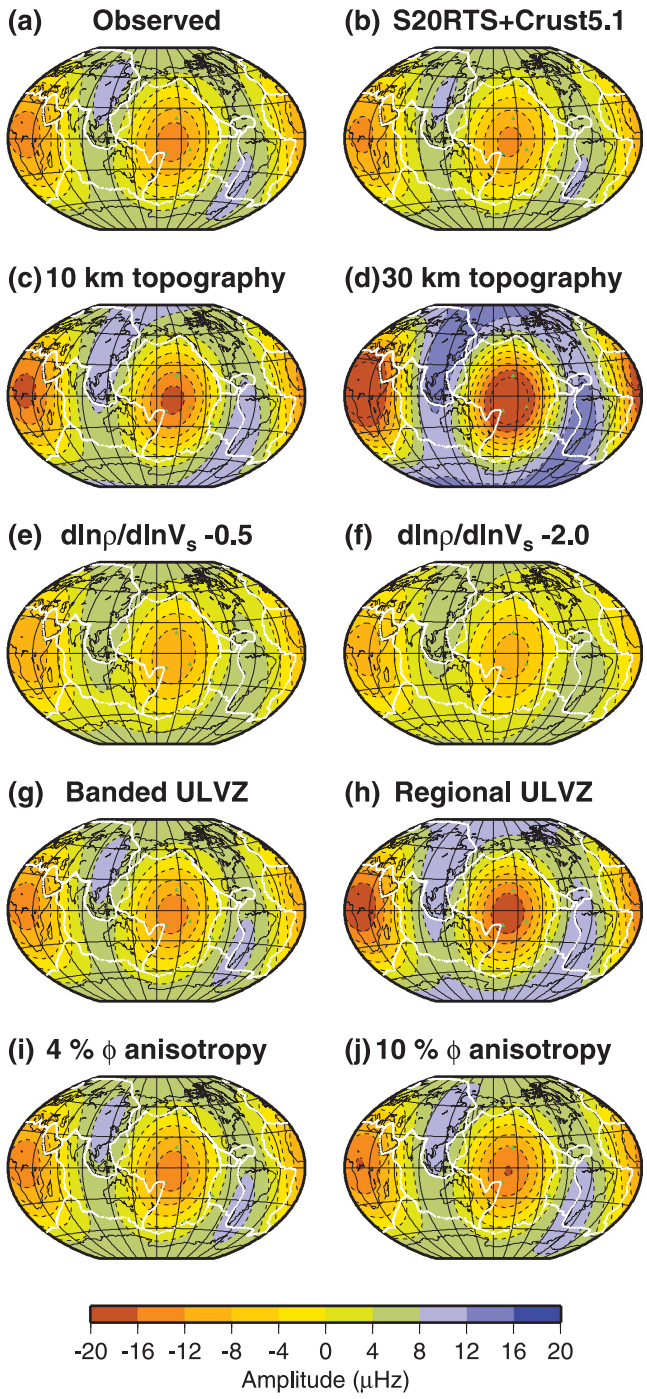

Figure 19. Observed and predicted self-coupled splitting functions for ${}_1S_{14}$ plotted for angular order 2. (a) Observed splitting function (Deuss *et al.* 2011). (b) Predicted splitting function for mantle model S20RTS and crustal model Crust5.1. (c and d) Predictions for S20RTS with added CMB topography model LGW1991SAT (Li *et al.* 1991b) scaled to 10 and 30 km. (e and f) Predictions for S20RTS with added scaling of $\delta\ln\rho/\delta\ln V_s = -0.5$ and $\delta\ln\rho/\delta\ln V_s = -2$ in a radial layer of 315 km. (g and h) Predictions for S20RTS with added 47 km thick banded and regional ULVZs with -30, -10 and $+10$ per cent for V_s, V_p and ρ respectively. (i and j) Predictions for S20RTS with added *P*-wave velocity anisotropy of 4 and 10 per cent.

discrepancy with the observations suggests that the extreme models in the right-hand side panels (Fig. 19d,f,h,j) are less likely. The trade-offs observed in the splitting function coefficients (Fig. 18) are also represented in the splitting function maps of Fig. 19; CMB topography and ULVZs have a similar effect on ${}_1S_{14}$ whereas $\delta\ln\rho/\delta\ln V_s$ has an opposite effect, with only a small contribution of anisotropy.

6 DISCUSSION

The influence of several lowermost mantle features has been investigated in this study. Although many of these structures have been observed extensively with body waves, normal mode studies have focused on larger scale inversions. Here, we have investigated what features normal modes are sensitive to and can resolve, as well as discuss possible trade-offs between the different structures.

Distinguishing different CMB topography patterns lies in the limit of what normal mode data can resolve. Of all the models presented in this study, the LGW1991SAT (Li *et al.* 1991b) shows the smallest L1 and L2 misfit for sensitive modes (excluding those with inner core sensitivity) in Table 1. Interestingly, this model was made using mode spectra so it is perhaps not surprising that it works best, even for a larger and newer data set. The effect of CMB topography amplitude is more significant and it should be possible to determine the amplitude within a few kilometres. This will help to constrain mantle convection models that generally overestimate the CMB topography amplitude (e.g. Forte *et al.* 1995; Lassak *et al.* 2010) compared to seismic data studies (e.g. Garcia & Souriau 2000; Sze & van der Hilst 2003). Our sensitivity study suggests that the CMB topography needs to be small, that is, less than <10 km peak-to-peak amplitude to be compatible with most normal mode data. If we only consider modes that are able to observe different CMB topography models (Table 1) with the exclusion of inner core sensitive modes, the allowed peak-to-peak amplitude is constrained to 5 km to fit the data within the given uncertainty.

Normal modes are also sensitive to small features, such as, banded ULVZs as long as they are thicker than 29 km and if the velocity anomalies are large enough. Given the fact that normal modes are sensitive to the entire Earth, this is remarkable and promising for future studies of ULVZs. However, their detection is limited by the presence of a long wavelength component in their distribution. This could be the case if they are dynamically linked to the edges of LLSVPs (McNamara *et al.* 2010). Our analysis provides, therefore, a starting point for future studies, which should concentrate on the modes that we identified to respond to ULVZ signals. As more data become available, it will be possible to focus on higher order degree coefficients to search for smaller scale lateral variations in ULVZ structure. With the current data, only regional ULVZ distributions up to 2 km thick or banded ULVZ structures up to 19 km thick are compatible with the data and the associated uncertainties, which is unfortunately also the limit of what the modes are able to observe. However, it is interesting that regional ULVZs of 19 km thick already show a significant effect on splitting function coefficients, so layers much thinner than 100 km can be identified with normal modes.

As scaling between *S*-wave velocity and density anomalies ($\delta\ln\rho/\delta\ln V_s$ ratio) has a relatively small effect on the normal mode splitting functions, this will be difficult to constrain given all the other possible structures in the lowermost mantle. Using only modes that display a significant sensitivity to the $\delta\ln\rho/\delta\ln V_s$ scaling in a simple forward modelling test, we show that the data is fitted best by a laterally varying pattern of this ratio. This simple test supports the

findings of previous studies (Ishii & Tromp 1999; Trampert *et al.* 2004) and implies a chemical origin for the LLSVPs. Lastly, introducing transverse vertical isotropy causes significant variations in the splitting functions data. The modes show small sensitivity to *S*-wave velocity anisotropy (ξ) and a strong trade-off exists between anisotropy in *P*-wave velocity anisotropy (ϕ) and anisotropy in incident angle (η) for a number of modes. Any upper limit estimates of anisotropy in Earth's D$''$ layer are prone to speculation due to the strong trade-offs between these different anisotropy parameters.

In addition to calculating the splitting function predictions with S20RTS as a 3-D mantle model we have calculated predictions using S40RTS. For most modes, these predictions show consistent variations with only a shift relative to the mantle model. In a few cases, for example, the third order overtones ($n = 3$), the predictions differ, leading to different inferences on D$''$ structure. Therefore, inversions for D$''$ structure should invert simultaneously for shallower mantle structure.

The observed anomalous splitting for inner core sensitive modes has been explained in terms of inner core anisotropy (Woodhouse *et al.* 1986) or potentially outer core structure with a minor effect of CMB topography (Romanowicz & Bréger 2000). We have demonstrated that many of the inner core sensitive modes show significant sensitivity to the pattern and amplitude of CMB topography. For some of these, including large CMB topography can account for nearly half of the observed anomalous splitting. However, such large topographies would not agree with the splitting function observations of mantle sensitive modes. Nonetheless, it is important to take CMB topography into account in inversions for inner core anisotropy and, preferentially, a joint inversion should be performed.

In this study, we have mainly shown results for degree 2 observability as this is the dominant structural degree found in the D$''$ region. Nevertheless, in our analysis we have calculated higher order degree splitting function coefficients up to a maximum of $s = 20$. These higher order degrees are affected by lowermost mantle structures in a similar way. However, uncertainties in the data are generally larger and coefficients have smaller absolute values for higher order degrees. Therefore, D$''$ anomalies have to be larger to be observable. Yet, inferences with regards to D$''$ sensitivity and trade-offs between structures remain the same.

In Table 2, results are given for higher order observability (eq. 4) for the models of Table 1. This table demonstrates that normal modes are sensitive to structures up to degree 6 for most models except for anisotropy in *S*-wave velocity (A_ξ) and banded ULVZs of 29 km (U_b). None of the inserted structures is anomalous enough to produce O_s-values larger than 1 for $s > 8$. However, even if the observability values are smaller than 1, signal due to D$''$ structure could be present in the synthetic data. It merely means that the uncertainties in the available data are too large for the structure to be observable. Nonetheless, it is worth pointing out that the current observability constraint is very conservative and will be more flexible in many situations when complementary data, such as body wave data, are available.

Table 2. Higher order observability of lowermost mantle structures. O_s values are calculated using eq. (4) for the structures indicated in Table 1; that is, the pattern (T_p) and amplitude (T_a) of CMB topography, regional (U_r) and banded (U_b) ULVZs, scaling ratios between $\delta\ln\rho$ and $\delta\ln V_s$ (S) and anisotropy in ϕ (A_ϕ), ξ (A_ξ) and η (A_η). In case at least one mode shows observability values larger than 1 for degree s, a cross is given for O_s. Although the CMB topography model of Li *et al.* (1991b) is only expanded up to degree 4, the model of Lassak *et al.* (2010) shows observability larger than 1 for degree 6 as well.

	T_p	T_a	U_r	U_b	S	A_ϕ	A_ξ	A_η
O_2	x	x	x	x	x	x	x	x
O_4	x	x	x	x	x	x	–	x
O_6	x	x	x	–	x	x	–	x
O_8	–	–	–	–	–	–	–	–

Although there are trade-offs between all the different lowermost mantle structures, the effect of $\delta\ln\rho/\delta\ln V_s$ scaling or anisotropy will generally be smaller than that of CMB topography or ULVZs. In addition, modes exist with only sensitivity to ULVZ structure and anisotropy and not CMB topography and vice verse. Inverting subsets of modes will, therefore, help to understand the nature of trade-offs in tomographical models. However, to constrain individual contributions of topography, ULVZs, anticorrelation and anisotropy, it is important to combine as many modes as possible.

We have demonstrated that normal modes are sensitive (within the limits of the current data) to structures up to at least structural degree 6. However, a good observability does not necessarily mean that these features are resolvable in tomographical inversions. To invert for structures in the D$''$ layer, it is hence vital to perform a joint inversion by combining normal mode and body wave data. The normal mode data act to constrain the long wavelength structures in the lowermost mantle and to resolve the main trade-offs between different features, whereas the body wave data are used to image the detailed structures. The results of this study, that normal modes are capable of observing the long wavelength components of D$''$ features, demonstrate that such joint inversions to image the Earth's deep mantle are viable.

7 CONCLUSIONS

We have investigated the sensitivity of normal modes to various structures in the lowermost mantle. We have demonstrated that the observability of normal modes to CMB topography, ULVZs, scaling of *S*-wave velocity and density perturbations and anisotropy is significant up to structural degree 6, despite the fact that normal modes are sensitive to the entire Earth.

We draw several inferences from our sensitivity analysis; (i) the pattern of CMB topography is more difficult to constrain than its peak-to-peak amplitude which should be less than 5 km to be compatible with most data. (ii) The effect of small scale ULVZs is strong enough to be identified in the splitting functions, and our analysis allows future studies to focus on identified modes that respond to ULVZ signals. (iii) Changing the ratio of density to shear wave velocity perturbations has a relatively small effect, but a simple test demonstrates that the $\delta\ln\rho/\delta\ln V_s$ ratio varies laterally, suggesting chemical variations. (iv) Anisotropy has a profound effect, especially for *P*-wave velocity anisotropy (ϕ) and variations in η, which display trade-offs for a large number of modes.

Trade-offs between many of these features exist and in any inversion of normal mode data, they should be taken into account. In addition, the 3-D mantle model can alter the inferences drawn from the data. We suggest that seismological studies of the D$''$ region focus on joint inversions employing both normal mode and body wave data. The normal modes are capable of contributing valuable insights in these inversions as long as the limitations in normal mode observability are kept in mind.

ACKNOWLEDGMENTS

We would like to thank Teresa Lassak, Rob van der Hilst and Alessandro Forte for providing their CMB topography models. We thank the Editor (Stephane Labrosse) and two anonymous reviewers for detailed comments, which greatly improved the manuscript. This research was funded by the European Research Council under the European Community's Seventh Framework Programme (FP7/2007-2013)/ERC grant agreement number 204995. PJK was also supported by the Nahum Scholarship in Physics and a Graduate Studentship, both from Pembroke College, Cambridge. Figures have been produced using the GMT software (Wessel & Smith 1998).

REFERENCES

Anderson, D., 1987. A seismic equation of state ii. shear properties and thermodynamics of the lower mantle, *Phys. Earth planet. Inter.,* **45**(4), 307–323.

Anderson, D., 1989. *Theory of the Earth,* Blackwell Scientific Publications, Malden, MA.

Aubert, J., Amit, H., Hulot, G. & Olson, P., 2008. Thermochemical flows couple the Earth's inner core growth to mantle heterogeneity, *Nature,* **454**(7205), 758–761.

Beghein, C., Trampert, J. & Van Heijst, H., 2006. Radial anisotropy in seismic reference models of the mantle, *J. geophys. Res.,* **111,** B02303.

Boschi, L. & Dziewonski, A., 2000. Whole Earth tomography from delay times of P, PcP, and PKP phases—lateral heterogeneities in the outer core or radial anisotropy in the mantle?, *J. geophys. Res.,* **105,** 13675–13696.

Castle, J., Creager, K., Winchester, J. & van der Hilst, R., 2000. Shear wave speeds at the base of the mantle, *J. geophys. Res.,* **105,** 21 543–21 557.

Chaloner, J., Thomas, C. & Rietbrock, A., 2009. P-and *S*-wave reflectors in D" beneath southeast Asia, *Geophys. J. Int.,* **179**(2), 1080–1092.

Dahlen, F. & Tromp, J., 1998. *Theoretical Global Seismology,* Princeton University Press Princeton, NJ.

Deschamps, F., Trampert, J. & Tackley, P., 2007. Thermo-chemical structure of the lower mantle: seismological evidence and consequences for geodynamics, in *Superplume: Beyond Plate Tectonics,* pp. 293–320, Springer, Dordrecht.

Deuss, A. & Woodhouse, J., 2001. Theoretical free-oscillation spectra: the importance of wide band coupling, *Geophys. J. Int.,* **146**(3), 833–842.

Deuss, A., Ritsema, J. & van Heijst, H., 2011. Splitting function measurements for Earth's longest period normal modes using recent large earthquakes, *Geophys. Res. Lett.,* **38**(4), L04303, doi:10.1029/2010GL046115.

Dziewonski, A. & Anderson, D., 1981. Preliminary reference Earth model, *Phys. Earth planet. Inter.,* **25**(4), 297–356.

Edmonds, A., 1960. *Angular Momentum in Quantum Mechanics,* Princeton University Press, Princeton, NJ.

Forte, A., 2007. Constraints on seismic models from other disciplines—implications for mantle dynamics and composition, *Treat. Geophys.,* **1,** 805–858.

Forte, A. & Mitrovica, J., 2001. Deep-mantle high-viscosity flow and thermochemical structure inferred from seismic and geodynamic data, *Nature,* **410**(6832), 1049–1056.

Forte, A., Mitrovica, J. & Woodward, R., 1995. Seismic-geodynamic determination of the origin of excess ellipticity of the core-mantle boundary, *Geophys. Res. Lett.,* **22**(9), 1013–1016.

Garcia, R. & Souriau, A., 2000. Amplitude of the core-mantle boundary topography estimated by stochastic analysis of core phases, *Phys. Earth planet. Inter.,* **117,** 345–359.

Garnero, E. & McNamara, A., 2008. Structure and dynamics of Earth's lower mantle, *Science,* **320**(5876), 626–628.

Garnero, E., Revenaugh, J., Williams, Q., Lay, T., Kellogg, L., 1998. Ultralow velocity zone at the core-mantle boundary, *Core-Mantle Bound. Region, Geodyn. Ser.,* **28,** 319–334.

Hager, B., Clayton, R., Richards, M., Comer, R. & Dziewonski, A., 1985. Lower mantle heterogeneity, dynamic topography and the geoid, *Nature,* **313**(6003), 541–545.

He, X. & Tromp, J., 1996. Normal-mode constraints on the structure of the earth, *J. geophys. Res.,* **101**(B9), 20053–20082.

Hide, R., Clayton, R., Hager, B., Spieth, M. & Voorhies, C., 1993. Topographic core-mantle coupling and fluctuations in the Earth's rotation, *Geophys. Monograph AGU,* **76,** 107–120.

Hirose, K., 2006. Postperovskite phase transition and its geophysical implications, *Rev. Geophys.,* **44**, RG3001, doi:10.1029/2005RG000186.

Hutko, A., Lay, T., Revenaugh, J. & Garnero, E., 2008. Anticorrelated seismic velocity anomalies from post-perovskite in the lowermost mantle, *Science*, **320**(5879), 1070–1074.

Ishii, M. & Tromp, J., 1999. Normal-mode and free-air gravity constraints on lateral variations in velocity and density of Earth's mantle, *Science,* **285**(5431), 1231–1236.

Jault, D. & Le Mouël, J., 1990. Core-mantle boundary shape: constraints inferred from the pressure torque acting between the core and the mantle, *Geophys. J. Int.,* **101**(1), 233–241.

Karato, S., 1993. Importance of anelasticity in the interpretation of seismic tomography, *Geophys. Res. Lett.,* **20**(15), 1623–1626.

Kendall, J. & Silver, P., 1996. Constraints from seismic anisotropy on the nature of the lowermost mantle, *Nature*, 381(6581), 409–412.

Kennett, B., Widiyantoro, S. & Van Der Hilst, R., 1998. Joint seismic tomography for bulk-sound and shear wavespeed in the earth's mantle, *J. geophys. Res.,* **103**(B6), 12469–12493.

Lassak, T., McNamara, A., Garnero, E. & Zhong, S., 2010. Core-mantle boundary topography as a possible constraint on lower mantle chemistry and dynamics, *Earth planet. Sci. Lett.,* **289,** 232–241.

Lay, T., 2007. Deep Earth structure—lower mantle and D″, *Treat. Geophys.,* **1,** 620–654.

Lay, T. & Garnero, E.J., 2011. Deep mantle seismic modeling and imaging, *Ann. Rev. Earth Planet Sci.,* **39,** 91–123.

Lay, T., Williams, Q. & Garnero, E., 1998. The core-mantle boundary layer and deep Earth dynamics, *Nature,* **392**(6675), 461–468.

Li, X., Giardini, D. & Woodhouse, J., 1991a. The relative amplitudes of mantle heterogeneity in P velocity, S velocity and density from free-oscillation data, *Geophys. J. Int.,* **105**(3), 649–657.

Li, X., Giardini, D. & Woodhouses, J., 1991b. Large-scale three-dimensional even-degree structure of the Earth from splitting of long-period normal modes, *J. geophys. Res.,* **96**(B1), 551–577.

Long, M., 2009. Complex anisotropy in D″ beneath the eastern Pacific from SKS-SKKS splitting discrepancies, *Earth planet. Sci. Lett.,* **283**(1–4), 181–189.

Love, A., 1927. *A Treatise on the Mathematical Theory of Elasticity,* Cambridge University Press, Cambridge.

McNamara, A., Garnero, E. & Rost, S., 2010. Tracking deep-mantle reservoirs with ultra-low-velocity zones, *Earth planet. Sci. Lett.,* **299**(1), 1–9.

Montagner, J., 1998. Where can seismic anisotropy be detected in the Earth's mantle? In boundary layers, *Pure appl. Geophys.,* **151**(2), 223–256.

Montagner, J. & Kennett, B., 1996. How to reconcile body-wave and normal-mode reference earth models, *Geophys. J. Int.,* **125**(1), 229–248.

Mooney, W., Laske, G. & Masters, T., 1998. CRUST 5.1: A global crustal model at 5 × 5°, *J. geophys. Res.,* **103**(B1), 727–747.

Moore, M., Garnero, E., Lay, T. & Williams, Q., 2004. Shear wave splitting and waveform complexity for lowermost mantle structures with low-velocity lamellae and transverse isotropy, *J. geophys. Res.,* **109,** B02319, doi:10.1029/2003JB002546.

Morelli, A. & Dziewonski, A., 1987. Topography of the core–mantle boundary and lateral homogeneity of the liquid core, *Nature,* **325,** 678–683.

Murakami, M., Hirose, K., Kawamura, K., Sata, N. & Ohishi, Y., 2004. Post-perovskite phase transition in $MgSiO_3$, *Science,* **304**(5672), 855.

Nowacki, A., Wookey, J. & Kendall, J., 2010. Deformation of the lowermost mantle from seismic anisotropy, *Nature,* **467**(7319), 1091–1094.

Oganov, A. & Ono, S., 2004. Theoretical and experimental evidence for a post-perovskite phase of MgSiO3 in Earth's D layer, *Nature,* **430**(6998), 445–448.

Panning, M. & Romanowicz, B., 2006. A three-dimensional radially anisotropic model of shear velocity in the whole mantle, *Geophys. J. Int.,* **167**(1), 361–379.

Resovsky, J. & Trampert, J., 2003. Using probabilistic seismic tomography to test mantle velocity-density relationships, *Earth planet. Sci. Lett.,* **215**(1–2), 121–134.

Ritsema, J., Heijst, H. & Woodhouse, J., 1999. Complex shear wave velocity structure imaged beneath Africa and Iceland, *Science,* **286**(5446), 1925–1928.

Ritsema, J., Deuss, A., van Heijst, H.J. & Woodhouse, J.H., 2011. S40rts: a degree-40 shear-velocity model for the mantle from new Rayleigh wave dispersion, teleseismic traveltime and normal-mode splitting function measurements, *Geophys. J. Int.,* **184**(3), 1223–1236.

Romanowicz, B. & Bréger, L., 2000. Anomalous splitting of free oscillations: a reevaluation of possible interpretations, *J. geophys. Res.,* **105**(B9), 21 559–21 578.

Rondenay, S., Cormier, V. & Van Ark, E., 2010. SKS and SPdKS sensitivity to two-dimensional ultralow-velocity zones, *J. geophys. Res.,* **115,** B04311, doi:10.1029/2009JB006733.

Rost, S., Garnero, E., Williams, Q. & Manga, M., 2005. Seismological constraints on a possible plume root at the core–mantle boundary, *Nature,* **435**(7042), 666–669.

Rost, S., Garnero, E., Thorne, M. & Hutko, A., 2010. On the absence of an ultralow-velocity zone in the North Pacific, *J. geophys. Res.,* **115**(B4), B04312, doi:10.1029/2009JB006420.

Simmons, N., Forte, A. & Grand, S., 2009. Joint seismic, geodynamic and mineral physical constraints on three-dimensional mantle heterogeneity: implications for the relative importance of thermal versus compositional heterogeneity, *Geophys. J. Int.,* **177**(5), 1284–1304.

Souriau, A., 2007. Deep Earth structure—the Earth's cores, *Treat. Geophys.,* **1,** 655–693.

Stixrude, L. & Karki, B., 2005. Structure and freezing of $MgSiO_3$ liquid in earth's lower mantle, *Science,* **310**(5746), 297–299.

Su, W. & Dziewonski, A., 1997. Simultaneous inversion for 3-D variations in shear and bulk velocity in the mantle, *Phys. Earth planet. Inter.,* **100**(1–4), 135–156.

Sze, E. & van der Hilst, R., 2003. Core mantle boundary topography from short period PcP, PKP, and PKKP data, *Phys. Earth planet. Inter.,* **135**(1), 27–46.

Thorne, M. & Garnero, E., 2004. Inferences on ultralow-velocity zone structure from a global analysis of SPdKS waves, *J. geophys. Res.,* **109**, doi:10.1029/2004JB003010.

Trampert, J., Deschamps, F., Resovsky, J. & Yuen, D., 2004. Probabilistic tomography maps chemical heterogeneities throughout the lower mantle, *Science,* **306**(5697), 853–856.

Van der Hilst, R., De Hoop, M., Wang, P., Shim, S., Ma, P. & Tenorio, L., 2007. Seismostratigraphy and thermal structure of Earth's core-mantle boundary region, *Science,* **315**(5820), 1813–1817.

Wenk, H., Cottaar, S., Tomé, C., McNamara, A. & Romanowicz, B., 2011. Deformation in the lowermost mantle: From polycrystal plasticity to seismic anisotropy, *Earth planet. Sci. Lett.*, **306**(1), 33–45.

Wessel, P. & Smith, W., 1998. New, improved version of the generic mapping tools released, *EOS, Trans. Am. geophys. Un.,* **79,** 579–579.

Williams, Q., Revenaugh, J. & Garnero, E., 1998. A correlation between ultra-low basal velocities in the mantle and hot spots, *Science,* **281**(5376), 546–549.

Woodhouse, J., 1980. The coupling and attenuation of nearly resonant multiplets in the Earth's free oscillation spectrum, *Geophys. J. R. astr. Soc.,* **61**(2), 261–283.

Woodhouse, J., Giardini, D. & Li, X., 1986. Evidence for inner core anisotropy from free oscillations, *Geophys. Res. Lett.,* **13**(13), 1549–1552.